Molecular Cell

Article

# Modulating synaptic glutamate receptors by targeting network nodes of the postsynaptic density condensate

## Graphical abstract

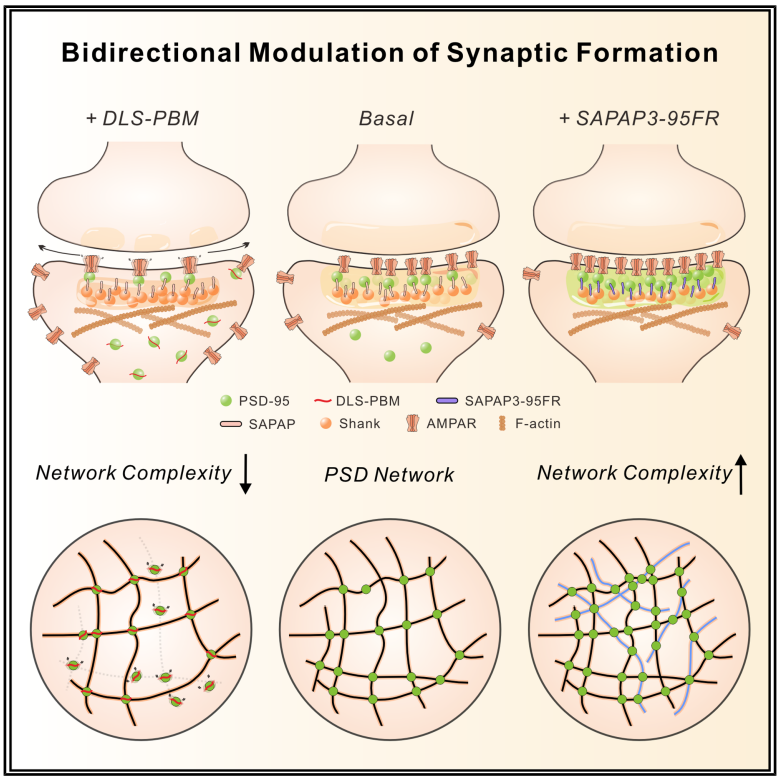


## Authors

Bowen Jia, Shihan Zhu, Zeyu Shen, ..., Roger A. Nicoll, Youming Lu, Mingjie Zhang

## Correspondence

zhangmj@sustech.edu.cn

## In brief

Jia et al. combined *in vitro* reconstitutions with experiments in living neurons to show that postsynaptic density (PSD) scaffold proteins interact with each other to form percolated molecular networks and drive formation of the PSD condensate. Regulatory factors target different interaction nodes in the condensate network to modulate synaptic functions.

## Highlights

- Specific interactions of scaffold proteins render percolated PSD condensate formation
- Regulatory factors modulate PSD condensate by targeting different network nodes
- PSD condensate is a complex system with emergent network properties
- Network properties of the PSD condensate are directly coupled to synaptic functions

Jia et al., 2025, Molecular Cell *85*, 3166–3183
August 21, 2025 
https://doi.org/10.1016/j.molcel.2025.07.017

CellPress

CellPress

Molecular Cell

Article

# Modulating synaptic glutamate receptors by targeting network nodes of the postsynaptic density condensate

Bowen Jia,[1,2,8] Shihan Zhu,[1,2,8] Zeyu Shen,[1,2,8] Xiumin Chen,[3,4] Hao Li,[5,6] Shuaizhu Zhao,[5,6] Qixu Cai,[7] Yu Wang,[1,2] Ziqi Wang,[1] Roger A. Nicoll,[4] Youming Lu,[5,6] and Mingjie Zhang[1,9,*]

[1]School of Life Sciences, Southern University of Science and Technology, Shenzhen 518055, China
[2]Division of Life Science, Hong Kong University of Science and Technology, Clear Water Bay, Kowloon, Hong Kong, China
[3]Department of Neurology and Institute of Neuroscience of Soochow University, Second Affiliated Hospital of Soochow University, Suzhou 215004, China
[4]Department of Cellular and Molecular Pharmacology, University of California, San Francisco, San Francisco, CA 94143, USA
[5]Department of Pathophysiology, School of Basic Medicine and Tongji Medical College, Huazhong University of Science and Technology, Wuhan 430030, China
[6]The Institute for Brain Research, Collaborative Innovation Center for Brain Science, Huazhong University of Science and Technology, Wuhan 430030, China
[7]State Key Laboratory of Vaccines for Infectious Diseases, School of Public Health, Xiamen University, Xiamen, Fujian 361102, China
[8]These authors contributed equally
[9]Lead contact
*Correspondence: zhangmj@sustech.edu.cn
https://doi.org/10.1016/j.molcel.2025.07.017

## SUMMARY

Biological condensates are assembled through phase separation and play critical roles in diverse cellular processes. Condensates in cells form percolated molecular networks via multi-valent interactions among biomolecules. How the network properties of a condensate are connected to its biological function is poorly understood. Using the neuronal postsynaptic density (PSD) condensate as a paradigm, we demonstrate thatbiological condensates can be bidirectionally modulated by strengthening or weakening different interaction nodes within the network. The clustering, mobility, and synaptic functions of AMPA receptors are exquisitely sensitive to alterations in the strength and complexity of the PSD condensate molecular network without changing the binding of the receptor to its direct downstream scaffold. Thus, biological condensates are complex systems with emergent network properties that are harnessed for cellular functions and in this case for synaptic plasticity.

## INTRODUCTION

Eukaryotic cells are highly compartmentalized. In addition to utilizing lipid membranes to build different forms of sub-cellular organelles, cells also contain another category of sub-cellular macromolecular assemblies that are not enclosed by lipid membranes. Such assemblies are referred to as membraneless organelles.[1–3] Membraneless organelles are formed via phase separation of interacting biomolecules, resulting in formation of condensed molecular assemblies surrounded by dilute intracellular molecular mixtures. Such condensed molecular assemblies are also called biological condensates.[4] Biological condensates play diverse roles in broad sub-cellular locations. For example, different presynaptic vesicle pools and postsynaptic densities (PSDs) of neuronal synapses are formed via phase separation[5–7]; stress granule condensates are assembled to sequester mRNAs under stress conditions[8–11]; rapid and specific responses to stimulation signals in immune systems are often mediated by immune signaling condensates[12–15]; the nucleolar structure is formed by layered organizations of condensates composed of proteins and different processed forms of ribosomal RNAs[16–18]; compartmentalization of different chromatin structures in the nucleus is also mediated by phase separation.[19–21] Abnormalities in biological condensates are linked to numerous diseases, including developmental defects, neurodegenerative diseases, immune disorders, cancers, etc.[22–26]

The basic principle governing formation of biological condensates is multivalent interaction-mediated formation of large molecular networks, which may or may not span the entire condensate at the mesoscale level (i.e., may or may not be percolated).[27–29] Both strong interactions via specific bindings of folded proteins/domains to their targets and weak interactions primarily mediated by intrinsically disordered regions/sequences (IDRs) contribute to formations of molecular networks in biological condensates. In PSD condensates, both the binding affinities and valences of the PSD scaffold proteins sensitively influence the

 

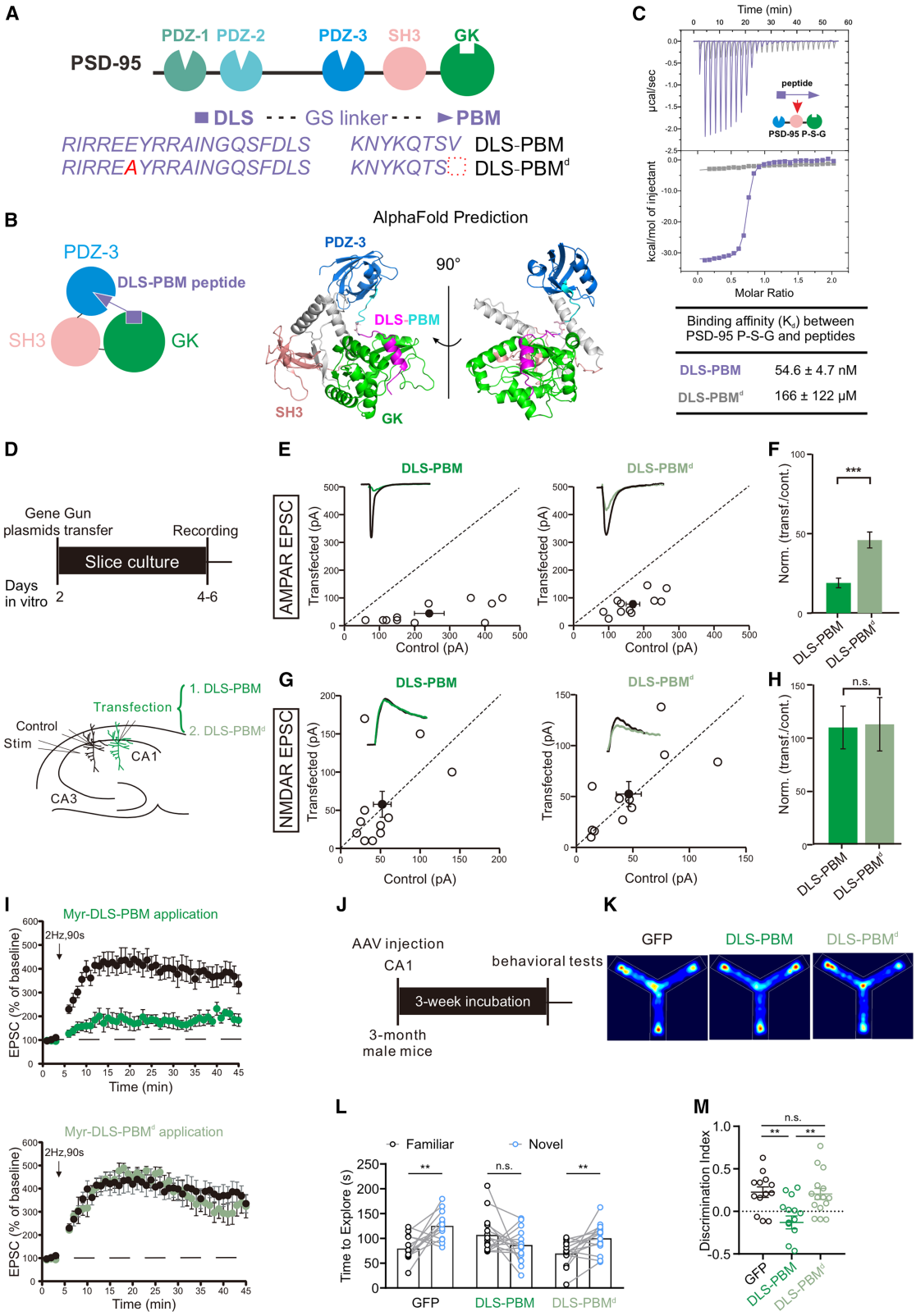


*(legend on next page)*

percolation level, network stability, and complexity of the molecular network of the condensates.[27,30,31] However, precise roles of each node in percolated network formation at the microscopic molecular level, in condensate formation at the mesoscopic level, and more importantly in the functions of condensates are understudied.

The PSD is a multiprotein molecular condensate beneath the postsynaptic plasma membrane in each excitatory synapse. The physical size of the PSD is near linearly correlated with the transmission strength of each synapse.[32–34] Molecularly, the size of the PSD is controlled by a collection of scaffold proteins including PSD-95, SAPAP, Shank, and Homer that can interact with each other via specific and multivalent protein-protein interactions.[7,35,36]

In this study, we used the reconstituted PSD condensate *in vitro* and PSDs in synapses of living neurons to characterize roles of different protein-protein interaction nodes on the stability of the percolated molecular network. We discovered that modulating nodes formed by interactions between scaffold proteins can effectively alter the network properties of the PSD condensate. Importantly, we found that altering network nodes that are away from the direct interaction node between AMPA receptor (AMPAR) and PSD-95 can dramatically alter the clustering, mobility, and functions of the receptor. Thus, the functions of a condensate and properties of molecules in the condensate are determined by the entire interaction network.

## RESULTS

### Designing a potent and specific pan-DLG blocking peptide

Since PSD-95 is a critical organizer of the PSD, we sought to design a peptide that can effectively block its scaffolding role in organizing the PSD. We targeted the PDZ3-SH3-GK (PSG) supramodule, which is known to bind directly to the lower layer scaffold protein SAPAP (a.k.a. GKAP).[37] To achieve high potency, we took advantage of the supramodular nature of PSD-95 PSG[38] by designing a bidentate peptide that can simultaneously engage its PDZ3 and GK modules (Figures 1A and 1B). The 8-residue extended PDZ-binding motif (PBM) is known to bind to PSD-95 PDZ3 with high affinity.[39] The GK domain targeting peptide (referred to as the "DLS" peptide) was extensively optimized and can bind to the GK domain with a $K_d \sim 1$ μM.[37,40] Based on the PSG supramodule structure,[41,42] linking the DLS peptide to the PBM peptide with a flexible Gly-Ser linker (GS-linker) generated a bidentate DLS-PBM peptide capable of synergistically targeting the PDZ3 and GK domains of PSD-95 (Figures 1A and 1B). We optimized the GS-linker length and found that a DLS-PBM peptide with a one-repeat GS-linker displayed the strongest binding to PSD-95 PSG ($K_d \sim 50$ nM; Figures 1C, S1A, and S1B). Figure 1B shows the structural model of PSD-95 PSG in complex with the optimized DLS-PBM peptide predicted by Alphafold2.[43] Indeed, the DLS-PBM peptide (DLS-PBM for short) and PSD-95 PSG complex formed a stable hetero-dimer (Figures S1C and S1D).

We next validated the specificity of DLS-PBM. First, we substituted the critical Glu residue that mimics the phosphor-Ser in the GK-binding peptides[37] with Ala and deleted the last Val residue of DLS-PBM (see Figure 1A for the design). The resulting mutant peptide displayed ~3,000-fold weakening in binding to PSD-95 PSG ($K_d \sim 166$ μM; Figure 1C). This mutant peptide is named DLS-PBM$^d$ (meaning the binding dead mutant) in our following studies. DLS-PBM also binds to PSD-93 and SAP102, both are the DLG family MAGUKs abundantly existing in PSDs, with high affinities (Figures S1E and S1F). In contrast,

**Figure 1. The designed DLS-PBM peptide impairs AMPAR transmission and brain function**

(A) Schematic diagram of the PSD-95 domain organization and the sequence of DLS-PBM. The Glu-to-Ala mutation (colored red) and deletion of the last Val are indicated in the DLS-PBM$^d$ sequence.

(B) Left: schematic binding mode of DLS-PBM to PSD-95 PSG. Right: a structural model showing DLS-PBM docked onto PSD-95 PSG.

(C) Isothermal titration calorimetry (ITC)-based measurement of the binding affinities of DLS-PBM (purple line) or DLS-PBM$^d$ (gray line) to PSD-95 PSG. In each ITC titration, 200 μM peptide was titrated into 20 μM of PSD-95 PSG.

(D) Schematic diagram showing the transfection and electrophysiological approaches. Control represents the WT, untransfected neurons.

(E) Scatterplots showing amplitudes of AMPAR EPSCs for single pairs (open circles) of control cells and cells expressing DLS-PBM or DLS-PBM$^d$ for 2–3 days ($n = 11$ pairs for each group). Filled circle indicates mean ± SEM. For left: control = 242 ± 42; DLS-PBM = 45 ± 14, $p < 0.0001$; for right: control = 170 ± 20; DLS-PBM$^d$ = 80 ± 10, $p < 0.0001$; Wilcoxon signed-rank test.

(F) Bar graph of ratios normalized to control (%) summarizing the mean ± SEM of AMPAR EPSCs of values represented in left of (E) (19 ± 3, $p < 0.0001$) and right of (E) (46 ± 5, $p < 0.0001$). Unpaired t test applied between DLS-PBM and DLS-PBM$^d$, $^{***}p < 0.001$.

(G) Scatterplots showing amplitudes of NMDAR EPSCs for single pairs (open circles) of control cells and cells expressing DLS-PBM or DLS-PBM$^d$ for 2–3 days ($n = 11$ pairs for each group). Filled circle indicates mean ± SEM. For left: control = 52 ± 11; DLS-PBM = 58 ± 17, $p > 0.05$; for right: control = 46 ± 11; DLS-PBM$^d$ = 52 ± 12, $p > 0.05$; Wilcoxon signed-rank test.

(H) Bar graph of ratios normalized to control (%) summarizing the mean ± SEM of NMDAR EPSCs of values represented in left of (G) (110 ± 21, $p > 0.05$) and right of (G) (113 ± 25, $p > 0.05$). n.s. not significant; unpaired t test applied between DLS-PBM and DLS-PBM$^d$.

(I) Plots showing mean ± SEM AMPAR EPSC amplitude of control (black) and 1 μM Myr-DLS-PBM peptide application (green) (top) or 1 μM Myr-DLS-PBM$^d$ peptide application (bottom). AMPAR EPSC amplitudes of pyramidal neurons were normalized to the mean amplitude before LTP induction (Myr-DLS-PBM peptide, $n = 8$; Myr-DLS-PBM$^d$ peptide, $n = 6$; control, $n = 8$, shared by both top and bottom).

(J) Schematic diagram showing the virus infection and the process for behavior tests.

(K) Representative heat maps showing the exploration patterns of mice expressing GFP, GFP-DLS-PBM, or GFP-DLS-PBM$^d$ during the Y-maze task. The upper left arm is the novel arm.

(L) Bar graphs showing the time spent exploring familiar (black) and novel (blue) arms in the Y-maze task. Data are presented as mean ± SEM ($n = 14$–16 number of mice for each group; $^{**}p < 0.01$; n.s., not significant; paired t test).

(M) The scatter plot showing the discrimination index for the Y-maze task, comparing GFP-, GFP-DLS-PBM-, and GFP-DLS-PBM$^d$-expressing groups. Data are presented as individual values with mean ± SEM ($n = 14$–16 number of mice for each group; $^{**}p < 0.01$; n.s., not significant; unpaired t test).

See also Figures S1 and S2.

DLS-PBM displayed a much weaker binding to MAGI-2 ($K_d$ ~ 4 μM, >70-fold weaker than binding to PSD-95; Figures S1E and S1F), which is a non-DLG MAGUK but also abundantly present in spines.[44] Thus, the designed DLS-PBM peptide can effectively and selectively block the binding of the DLG MAGUKs to SAPAPs.

## DLS-PBM impairs synaptic transmission and plasticity

We next asked whether disrupting the PSD-95-organized scaffold network in the PSD by DLS-PBM might alter synaptic functions. We expressed the GFP-fused DLS-PBM peptide or the DLS-PBM$^d$ peptide by biolistically delivering expression plasmids to the CA1 region of cultured rat brain slices. Simultaneous whole-cell recordings were made from a control cell and a transfected cell in each experiment, and their responses to a common synaptic input were compared (Figure 1D). In neurons expressing GFP-DLS-PBM, AMPAR basal transmission was reduced by ~80% (Figures 1E and 1F). Although GFP-DLS-PBM$^d$ also weakened AMPAR transmission possibly due to the remaining weak interaction with PSD-95, the reduction of the amplitude was significantly smaller than GFP-DLS-PBM (Figures 1E and 1F). Importantly, NMDA-receptor-mediated synaptic responses were not changed in synapses expressing both peptides (Figures 1G and 1H), indicating that the changes observed in the AMPAR transmissions specifically resulted from alterations of AMPAR signaling complex reorganization.

We next investigated whether synaptic plasticity was altered by DLS-PBM. Long-term potentiation (LTP) could be normally induced in acute brain slices with a standard LTP-inducing paradigm. However, in the presence of cell-permeable myristoylated DLS-PBM peptide (Myr-DLS-PBM), LTP was greatly reduced (Figure 1I, top). In contrast, application of Myr-DLS-PBM$^d$ did not cause abnormality on the LTP induction and maintenance (Figure 1I, bottom). Hence, we conclude that the binding of PSD-95 to SAPAP is essential for synaptic transmission and plasticity.

As synaptic plasticity is the underlying mechanism for learning and memory, we next evaluated learning and memory of mice expressing the blocking peptide. We used adeno-associated virus (AAV) to deliver GFP, GFP-DLS-PBM, and GFP-DLS-PBM$^d$ individually into mice CA1 region of hippocampus (Figures 1J and S2A). After 3 weeks of expression, the mice were subjected to behavioral tests. In novel object recognition assay, all mice spent equal time on two familiar objects (Figure S2B), indicating that the viral infection did not impair the basic functions (Figures S2B–S2D). In next round, mice expressing GFP control and GFP-DLS-PBM$^d$ spent more time on the novel object (Figure S2E). However, mice expressing GFP-DLS-PBM could not recognize the novel object, suggesting deficits on cognitive memory (Figures S2E–S2G). Consistently, in the Y-maze test, mice expressing GFP or GFP-DLS-PBM$^d$ spent more time on the novel arm (Figure 1K, left arm), but the mice expressing GFP-DLS-PBM did not (Figures 1K–1M). Therefore, disrupting the interaction between PSD-95 and SAPAP by DLS-PBM severely impaired learning and memory in the rodent models.

## AMPARs are destabilized by the DLS-PBM peptide

Since the electrophysiology experiments have indicated weakening of AMPAR basal transmission and disruption of LTP, we directly investigated the impact of DLS-PBM on synaptic AMPAR. We immuno-stained endogenous AMPAR subunit GluA1 and quantified GluA1 enrichment in dendritic spines of neurons expressing GFP-tagged DLS-PBM peptide (Figures 2A and 2B). Overexpression of GFP-DLS-PBM led to ~50% decrease of GluA1 spine enrichment compared with the GFP and DLS-PBM$^d$ groups (Figure 2B), indicating that DLS-PBM can directly perturb the synaptic targeting and clustering of GluA1.

We next monitored endogenous synaptic AMPAR mobilities upon expression of DLS-PBM in living neurons by live cell single-molecule tracking (SMT) (Figure 2C). Consistent with an earlier study,[45] in neurons expressing the GFP vector or GFP-DLS-PBM$^d$, the trajectories for GluA1 were confined in a small region with very occasional switching to higher mobilities and the overall mobilities of GluA1 molecules were very low, indicating that most of the AMPARs in synaptic spines are stably integrated into PSDs (Figures 2D–2F). In contrast, in neurons expressing GFP-DLS-PBM, the receptors explored a significantly larger area with higher diffusion speeds, indicating that the AMPARs were much more mobile in these synapses (Figures 2D–2F). Therefore, the increased mobility and decreased clustering of AMPAR in neurons expressing or applied with DLS-PBM led to impaired AMPAR basal transmission and defective LTP of synapses shown in Figure 1.

## DLS-PBM disperses PSD core proteins out of dendritic spines

The above results suggested the strong perturbation of the AMPAR basal transmission and the receptor clustering within PSDs by DLS-PBM. However, DLS-PBM does not directly interfere with the interaction between AMPAR and PSD-95, as AMPAR binds to the PDZ1-2 tandem of PSD-95.[46] We thus investigated the molecular and cellular basis underlying DLS-PBM-induced synaptic functional changes. We first performed a cellular phenotypic screening by co-expressing DLS-PBM with one of the following GFP-tagged PSD proteins each time in cultured hippocampal neurons: PSD-95 and an AMPAR auxiliary subunit Stargazin (Stg), representing the PSD core proteins; SAPAP1, Shank3, and Homer1, representing scaffold proteins in the PSD pallium.[47,48] As DLS-PBM blocks the interaction between SAPAPs and PSD-95, we expected to observe localization changes of the PSD pallium proteins. We unexpectedly observed that both Stg and PSD-95 were dramatically dispersed from spines by DLS-PBM. In contrast, the spine enrichments of the three PSD pallium proteins (SAPAP1, Shank3, and Homer1) were minimally changed (Figures 3A and 3B). This can be explained by earlier findings showing that these three pallium scaffold proteins can still form percolated molecular networks,[7,49] and the formed condensate can interact with spine actin cytoskeletons.[50] In the control group, expression of the DLS-PBM$^d$ peptide had no impact on the spine localization of all five PSD proteins (Figures 3A and 3B). We further evaluated the impact of DLS-PBM on the synaptic localizations of endogenous PSD scaffold proteins by immunostaining. Expression of GFP-tagged DLS-PBM peptide caused dramatic dispersion of endogenous PSD-95 from the spines but had no impact on the spine localization of the Shank family scaffold proteins (Figures 3C and 3D).

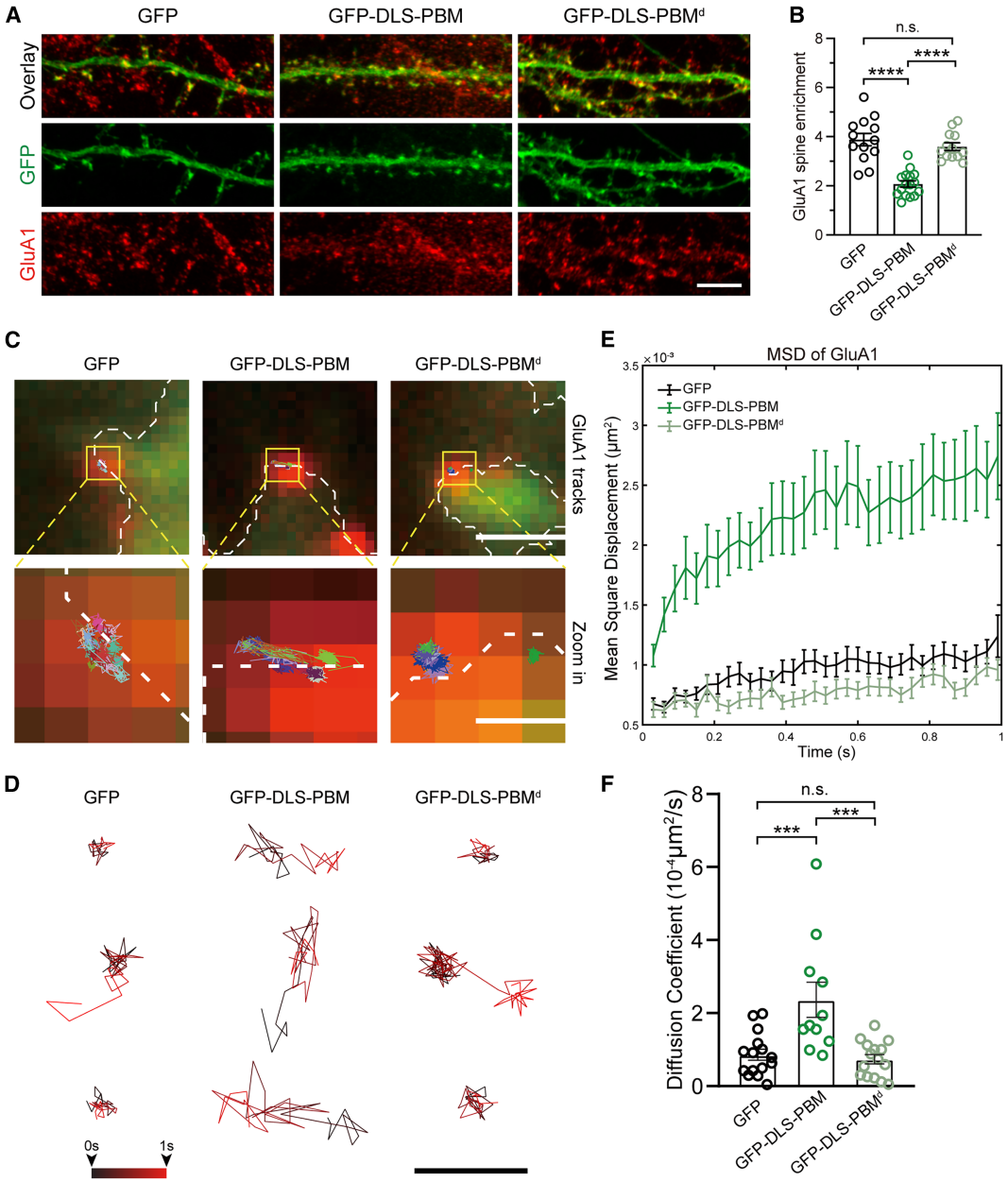


**Figure 2. DLS-PBM peptide decreases AMAPR enrichment and increases AMPAR mobility in the PSD of living neurons**

(A) Representative images showing the endogenous staining of AMPAR subunit GluA1in neurons expressing GFP, GFP-DLS-PBM or GFP-DLS-PBM$^{d}$. Scale bar: 5 μm.

(B) Quantification of GluA1 spine enrichment fold from (A). Data are shown as mean ± SEM. $n$ = 13 (GFP), 16 (GFP-DLS-PBM), 13 (GFP-DLS-PBM$^{d}$) neurons with 30–50 spines per neuron from four independent batches. One-way ANOVA followed by Tukey's post hoc test, ****$p < 0.0001$, n.s., not significant.

(C) Representative images showing the surface staining of GluA1 and its trajectories in spines from neurons expressing GFP, GFP-DLS-PBM, or GFP-DLS-PBM$^{d}$, respectively. White dashed lines show the outline of individual spines with GFP signals (green), and red represents the epifluorescence of the GluA1 signal. Zoom-in images with sample trajectories of GluA1 movements are shown in the bottom panels. Each color represents a single trajectory. Scale bar: 1 μm (top) and 200 nm (bottom).

(D) Three representative GluA1 trajectories each with 1 s time duration from neurons expressing GFP, GFP-DLS-PBM, or GFP-DLS-PBM$^{d}$, respectively. Scale bar: 100 nm.

(E) Mean square displacement (MSD) analysis of trajectories from neurons expressing GFP, GFP-DLS-PBM or GFP-DLS-PBM$^{d}$, respectively. Data are shown as mean ± SEM. $n$ = 10,884/13,124/9,428 trajectories from 20/26/22 neurons from three independent batches for GFP/GFP-DLS-PBM/GFP-DLS-PBM$^{d}$, respectively.

(F) Diffusion coefficient of GluA1 in synapses of individual neurons derived from the experiments shown in (E). Error bar indicates ± SEM. One-way ANOVA followed by Tukey's post hoc test, ***$p < 0.001$, n.s., not significant.

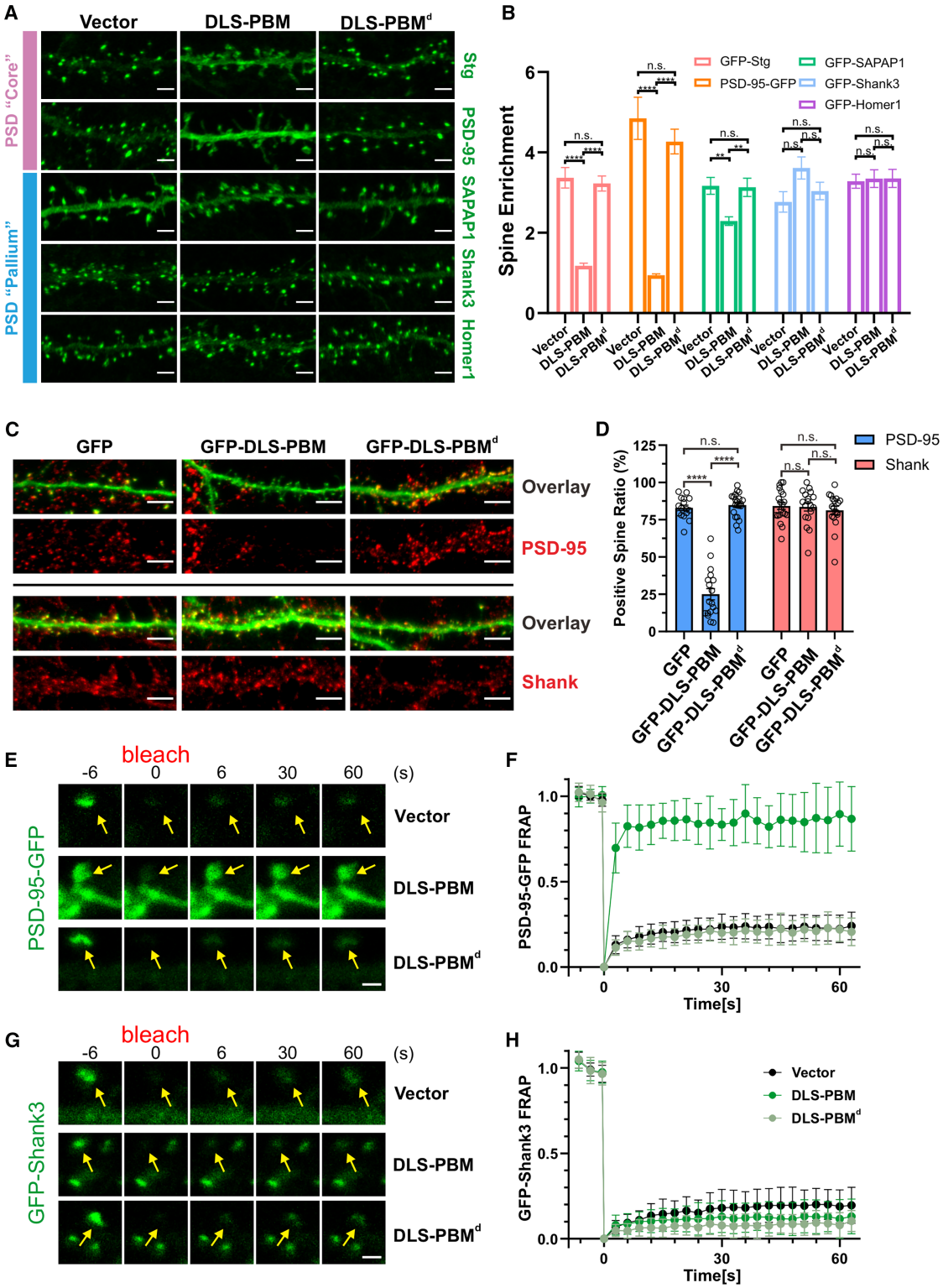


**Figure 3. DLS-PBM peptide selectively weakens the PSD core but not the PSD pallium**

(A) Representative images showing the spine localization of expressed PSD core proteins and PSD pallium proteins co-expressed with mCherry, mCherry-DLS-PBM, or mCherry-DLS-PBM$^{d}$. Scale bar: 5 μm.

(B) Quantitative analysis of spine enrichment of expressed PSD proteins in individual groups. Error bars indicate ± SEM. *n* equals number of neurons with 20–30 spines per neuron, *n* = 23 (GFP), 15 (DLS-PBM), 20 (DLS-PBM$^{d}$) for GFP-Stg; *n* = 15, 15, 20 for PSD-95-GFP; *n* = 18, 18, 18 for GFP-SAPAP1; *n* = 13, 15, 15 for

*(legend continued on next page)*

In mature neurons, PSD-95 are assembled into stable PSD condensates and its mobility is very low.[51,52] Fluorescence recovery after photobleaching (FRAP) experiments confirmed that signals of GFP-tagged PSD-95 in spines recovered very slowly (Figures 3E and 3F). In sharp contrast, the signal of PSD-95-GFP in spines recovered rapidly when the neurons were co-expressed with mCherry-DLS-PBM (Figures 3E and 3F). Again, the mobilities of Shank3 did not change upon expression of DLS-PBM (Figures 3G and 3H). We also checked that the PSD enrichment of SynGAP, a major PSD protein and synaptic plasticity regulator binding to PSD-95,[53–56] was not obviously altered by the DLS-PBM peptide expression (Figures S3A and S3B). Thus, the DLS-PBM peptide-induced dispersion of AMPARs and PSD-95 from the PSD core chiefly accounts for the impaired synaptic functions.

## Network complexity and stability of PSD condensate determine the mobilities of AMPARs

DLS-PBM can effectively disrupt the interaction between PSD-95 and SAPAP (Figure 1) but does not directly alter the interaction between Stg and PSD-95 or disturb the PSD core condensates formation (see the scheme in Figure 4A). Nonetheless, the peptide dramatically weakened the clustering of the PSD core components (Figures 2 and 3). To elucidate the underlying mechanism, we employed a reconstituted PSD platform with major proteins from both the PSD core and the PSD pallium (Figure 4A).[7] Our earlier SMT experiments[27] and very recent atomic force microscopy (AFM) studies[31] demonstrated that the reconstituted PSD condensate formed percolated molecular networks with unique viscoelastic material properties. We first confirmed that DLS-PBM dispersed PSD-95 from the reconstituted condensate composed of PSD-95, SAPAP1 (GKAP), Shank3, and Homer2, but the peptide did not alter the PSD pallium condensate formation (Figure S4A). Addition of DLS-PBM to the 5× PSD condensate formed by five proteins shown in Figure 4A led to formation of two distinct phases arranged in a phase-to-phase pattern, with one phase composed of PSD core proteins PSD-95 and Stg and the other phase formed by the three PSD pallium proteins (Figure 4B). DLS-PBM also weakened the PSD condensate formed on the surface of lipid membranes (Figure S4B). Thus, DLS-PBM can uncouple the upper layer and lower layer of the PSD condensates by disrupting the interaction between PSD-95 and SAPAP.

The DLS-PBM-uncoupled upper layer PSD-95 and Stg mixture could still form condensates[46] (Figure 4B). Why is it then that PSD-95 and Stg could be easily dispersed from synapses by the DLS-PBM? To address this, we compared motion properties of PSD-95 and Stg_CT in the condensates formed only by PSD-95 and Stg_CT (denoted as 2× PSD or "PSD core") or by 5× PSD (or "PSD core + pallium") by SMT. In 5× PSD, both Stg_CT and PSD-95 molecules spent most of the time in immobile state and occasionally could switch to mobile state (Figures 4C and 4D, right), reflecting that these two molecules together with the other components in the condensate formed stable and percolated network.[27,30,31] In 2× PSD, the overall mobility and the proportion of Stg_CT and PSD-95 in the mobile state in the condensed phase are significantly increased, though the 2× PSD condensate still formed percolated network evidenced by the two distinct motion state properties of the molecules in the condensate (Figures 4C and 4D, left). The diffusion behavior of Stg and PSD-95 in the 2× PSD condensate mirrors the increased mobilities of GluA1 and PSD-95 in synapses of neurons expressing DLS-PBM (Figures 2C–2F). We also showed that addition of SAPAP1/GKAP to the 2× PSD core (3× PSD) condensate did not dramatically change the diffusion behavior of Stg and PSD-95 (Figures 4C and 4D, middle; quantified in Figures 4E, 4F, S4C, and S4D), as SAPAP1 is a monomer and acting as a client of the 2× PSD condensate. This result further verifies that coupling of the PSD core and pallium condensates together, instead of only direct SAPAP binding to PSD-95, is responsible for the slower motions of Stg_CT and PSD-95 in the 5× PSD condensate. The above data collectively indicate that the network complexity directly determines the mobilities of each molecular component in a condensate (Figure 4G).

If the above interpretation stands, we predicted that the mobility of PSD-95 would also change if we modulated another interaction node in the PSD protein network. To test this prediction, we used Homer1a, which is the monomeric isoform of Homer1 and functions as an immediate-early gene product capable of downregulating PSD formation.[57–59] As Homer1a only contains the Shank-binding EVH1 domain, this monomeric protein

GFP-Shank3; $n$ = 25, 23, 22 for GFP-Homer1. Neurons were collected from three independent batches except for the GFP-Shank3 group with two independent batches of cultures. One-way ANOVA followed by Tukey's post hoc test, $^{**}p < 0.01$, $^{****}p < 0.0001$, n.s., not significant.

(C) Representative images showing the immunostaining of endogenous PSD-95 and pan-Shank in neurons expressing GFP, GFP-DLS-PBM, or GFP-DLS-PBM$^{d}$, respectively. Scale bar: 5 μm.

(D) Quantitative analysis of percentages of PSD-95 signal-positive spines and Shank-positive spines in individual groups. Error bars indicate ± SEM. $n$ equals number of neurons with 30–50 spines per neuron. $n$ = 16 (GFP),18 (GFP-DLS-PBM), 21 (GFP-DLS-PBM$^{d}$) for PSD-95 staining and 20, 18, 18 for pan-Shank staining from three independent batches of cultures. One-way ANOVA followed by Tukey's post hoc test, $^{****}p < 0.0001$, n.s., not significant.

(E) Representative time-lapse images showing the fluorescence recovery of PSD-95-GFP after photobleaching in dendritic spines of neurons co-expressing mCherry, mCherry-DLS-PBM or mCherry-DLS-PBM$^{d}$, respectively. Scale bar: 1 μm.

(F) Quantitative analysis of results in (E). Data are shown as mean ± SEM. Black curve, mCherry ($n$ = 23 spines of 11 neurons from four independent batches); green curve, mCherry-DLS-PBM ($n$ = 22 spines of 11 neurons from four independent batches); gray green curve, mCherry-DLS-PBM$^{d}$ ($n$ = 17 spines of eight neurons from three independent batches).

(G) Representative time-lapse images showing the fluorescence recovery of GFP-Shank3 after photobleaching in dendritic spines of neurons co-expressing mCherry, mCherry-DLS-PBM or mCherry-DLS-PBM$^{d}$, respectively. Scale bar: 1 μm.

(H) Quantitative analysis of results in (G). Data are shown as mean ± SEM. Black curve, mCherry ($n$ = 33 spines of 12 neurons from four independent batches); green curve, mCherry-DLS-PBM ($n$ = 23 spines of 12 neurons from four independent batches); gray curve, mCherry-DLS-PBM$^{d}$ ($n$ = 22 spines of 12 neurons from four independent batches).

See also Figure S3.

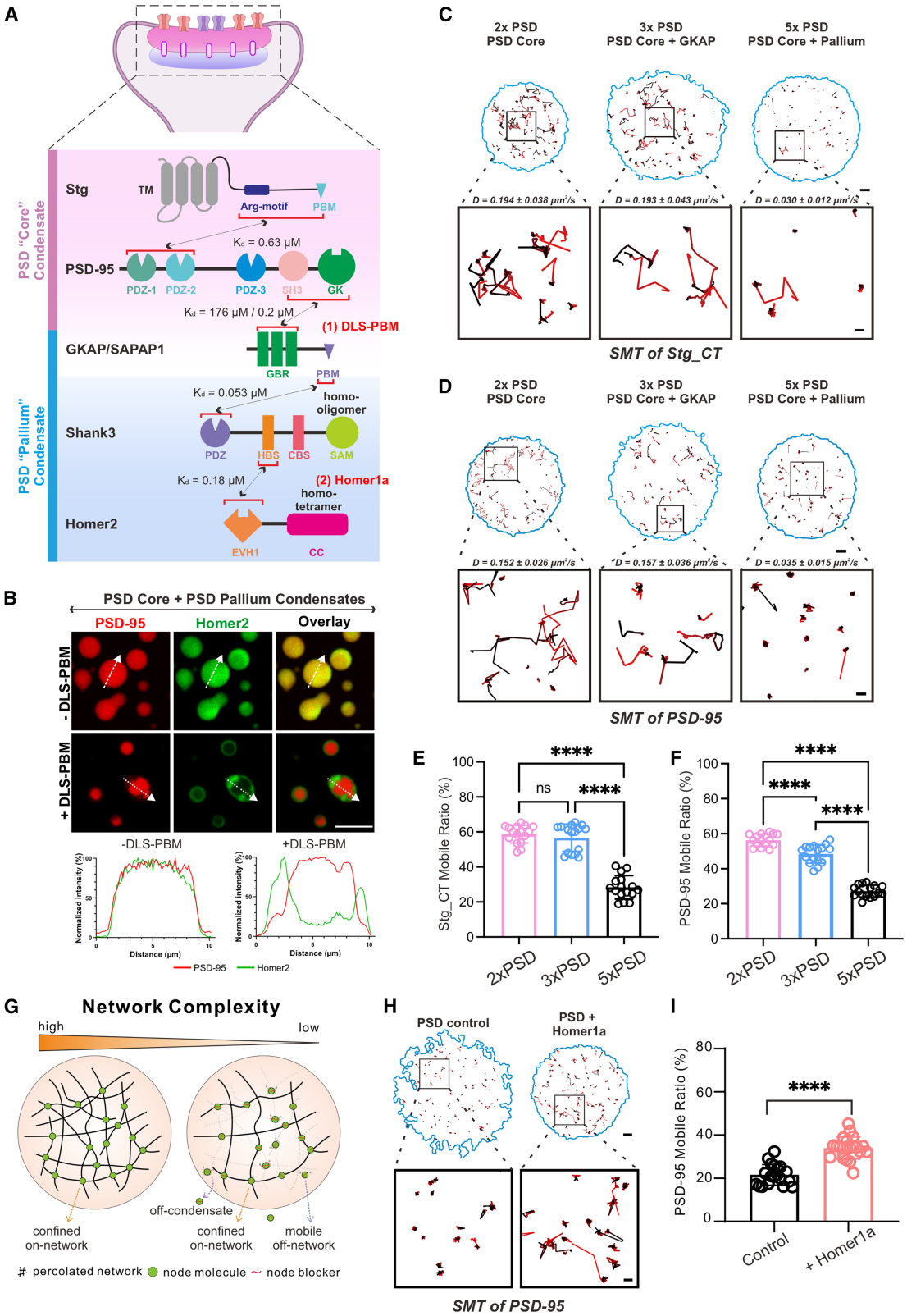


(legend on next page)

can effectively block the Shank/Homer interaction node and reduce the PSD network complexity (Figure 4A). Consistent with our prediction, application of Homer1a in the 5× PSD condensate also led to increased mobility of PSD-95 and Stg_CT (Figures 4H, 4I, S4E, and S4F).

## PSD-95.FingR intrabody blocks the binding of SAPAP to PSD-95 GK

PSD-95.FingR (denoted as 95FR) is a PSD-95-binding intrabody widely used for visualization of PSD-95 in living neurons.[60] 95FR binds to the PSG supramodule of PSD-95 strongly with a nanomolar affinity.[30] Here, we further mapped that 95FR binds to the PSD-95 GK domain with $K_d \sim 2$ nM (Figures 5A and S5A). Importantly, 95FR binds to the GK domains of the DLG MAGUKs (PSD-95, PSD-93, SAP97, and SAP102) but not to other synaptic MAGUKs (MPP2, MPP5, CASK, and MAGI-2) (Figures 5B left and S5), revealing that 95FR is a specific and potent DLG GK domain binder.

We solved the crystal structure of PSD-95_GK in complex with 95FR at 1.93 Å resolution (Figure 5C; Table 1). 95FR adopts a canonical fibronectin type III fold (Figure S6A). The β2-β3 and β6-β7 loops of 95FR bind to a pocket formed by the GMP-binding (GMP-BD) and the CORE/LID subdomains of PSD-95_GK (Figures 5C, 5D, and S6B). Analysis of the complex structure, together with amino acid sequence alignment of GKs from different MAGUKs, revealed the mechanistic basis governing the specific binding of 95FR to GKs from the DLG MAGUKs (Figures 5C, 5D, and S6 and additional text in Figure S6 legend).

We validated the structure of the PSD-95_GK/95FR complex by generating a series of mutations in the β6-β7 loop of 95FR (Figures 5B right and S6E–S6J). One 95FR mutant (F72E, with Phe72 replaced by Glu) completely disrupted the binding of the intrabody to PSD-95_GK (Figure 5A). When expressed in hippocampal neurons, 95FR_WT (wild type) was enriched in dendritic spines but 95FR_F72E was diffused in dendritic spines and shafts (Figures S6K–S6M).

Superposition of the PSD-95_GK/95FR complex structure with the PSD-95_GK/pi-SAPAP1-R2 complex structure[37] revealed that the β6-β7 loop of 95FR and pi-SAPAP1-R2-binding sites on the GK domain are overlapped (Figure 5E), indicating that the binding of the two targets to PSD-95_GK are mutually exclusive. Given that 95FR binds to PSD-95_GK with a significantly higher affinity than pi-SAPAP1-R2 ($K_d$ values of 2 nM versus ∼100 nM; Zhu et al.[37]; Figure 5A), we predicted that 95FR could effectively block PSD-95_GK from binding to pi-SAPAP. This prediction was confirmed by analytical gel-filtration chromatography, in which only the 95FR/PSD-95_PSG complex was formed when 95FR, pGKAP, and PSD-95_PSG were mixed together (Figure 5F). Thus, when overexpressed in neurons, 95FR should be able to effectively and specifically block the interaction between PSD-95 (or other DLG MAGUKs) and SAPAPs without interfering with any PDZ-domain-mediated target bindings of PSD-95 (e.g., bindings of AMPARs or SynGAP to PSD-95).

## Uncoupling of the PSD-95/SAPAP interaction by 95FR weakens synaptic AMPAR clustering

Indeed, neurons overexpressing 95FR_WT (95FR_WT_OE) showed dramatic PSD-95 and GluA1 dispersions from dendritic spines. In contrast, overexpression of the 95FR_F72E mutant (95FR_F72E_OE) had no impact on the clustering of PSD-95 and GluA1 in synapses (Figures 5G and 5I). Shank and SynGAP were not influenced by 95FR_WT_OE (Figures 5H, S3C, and S3D). The result above, together with the data in Figures 1, 2, 3, and 4, collectively demonstrated that uncoupling of the PSD core and pallium condensates weakens the PSD network and results in synaptic defects.

The 95FR was designed as a labeling tool for imaging endogenous PSD-95 by fusing with the CCR5TC element (95FR-GFP-CCR5TC) to limit the intrabody expression.[60] We confirmed that limited expression of 95FR using the 95FR-GFP-CCR5TC cassette did not induce significant changes to the synaptic

**Figure 4. DLS-PBM peptide uncouples the PSD core and pallium and destabilizes the PSD molecular network**

(A) Schematic diagram showing the components in the reconstituted PSD condensates and their interaction details. Black arrows indicate the measured binding affinities of the interactions. (1) Represents the targeting of the PSD-95/SAPAP interaction node by DLS-PBM, and (2) represents the targeting of the Shank/Homer interaction node by Homer1a. The binding affinity ($K_d$) between PSD-95 and GKAP is 176 μM (non-phosphorylated GKAP) or 0.2 μM (phosphorylated GKAP).

(B) Representative images showing the co-localization of PSD core condensate (indicated by Cy3-PSD-95) and PSD pallium condensate (indicated by iFluor 488-Homer2) in the absence of DLS-PBM (up). Addition of DLS-PBM caused segregation of the core and pallium condensates. In this experiment, 20 Stg, 20 PSD-95 (Cy3 labeling ratio of 1%), 5 pGKAP, 5 GKAP, 10 Shank3, and 10 Homer2 (iFluor 488 labeling ratio of 1%) all in μM were used to reconstitute the PSD condensate (5× PSD); DLS-PBM peptide was at 50 μM. Bottom, line-scanning analysis of fluorescent intensities of labeled proteins. Scale bar: 10 μm.

(C and D) Representative images showing the trajectories of Stg_CT (C) and PSD-95 (D) (Cy3 labeling ratio of 0.035%) from 2× PSD (20 Stg and 20 PSD-95), 3× PSD (20 Stg, 20 PSD-95, 5 pGKAP, 5 GKAP), and 5× PSD (20 Stg, 20 PSD-95, 5 pGKAP, 5 GKAP, 10 Shank3 and 10 Homer2), all in μM. Zoom-in images are used to show examples of single-molecule trajectories. The derived average apparent diffusion coefficient of each tracked molecule is marked above the representative zoom-in images as mean ± SD. Scale bar: 1 μm (up), 250 nm (bottom).

(E and F) Quantification of the mobile ratios of Stg_CT (E) and PSD-95 (F) in the three types of condensates based on single-molecule trajectories from (C) and (D). Error bar indicates ± SD. $n = 16$ droplets for both groups. One-way ANOVA followed by Tukey's post hoc test, ****$p < 0.0001$; ns, not significant.

(G) Schematic diagram showing the blockage of a key node on the percolated molecular network by a specific node blocker leads to a network complexity decrease. Consequently, more molecules are off the network, thereby displaying higher mobilities and less enriched in the condensate.

(H) Representative images showing the single-molecule trajectories of PSD-95 (Cy3 labeling ratio of 0.035%) from 5× PSD control (10 Stg, 10 PSD-95, 10 pGKAP, 10 Shank3-ME, and 10 Homer2) or 5× PSD adding 250 Homer1a, all in μM. Zoom-in images are used to show examples of single-molecule trajectories. Scale bar: 1 μm (up), 250 nm (bottom).

(I) Quantification of mobile ratios of PSD-95 derived from the single-molecule trajectories in (H). Error bar indicates ± SD. $n = 19, 21$ condensates for PSD control and PSD with Homer1a, respectively. Unpaired t test, ****$p < 0.0001$.

See also Figure S4. (A) was drawn using BioRender (https://www.biorender.com).

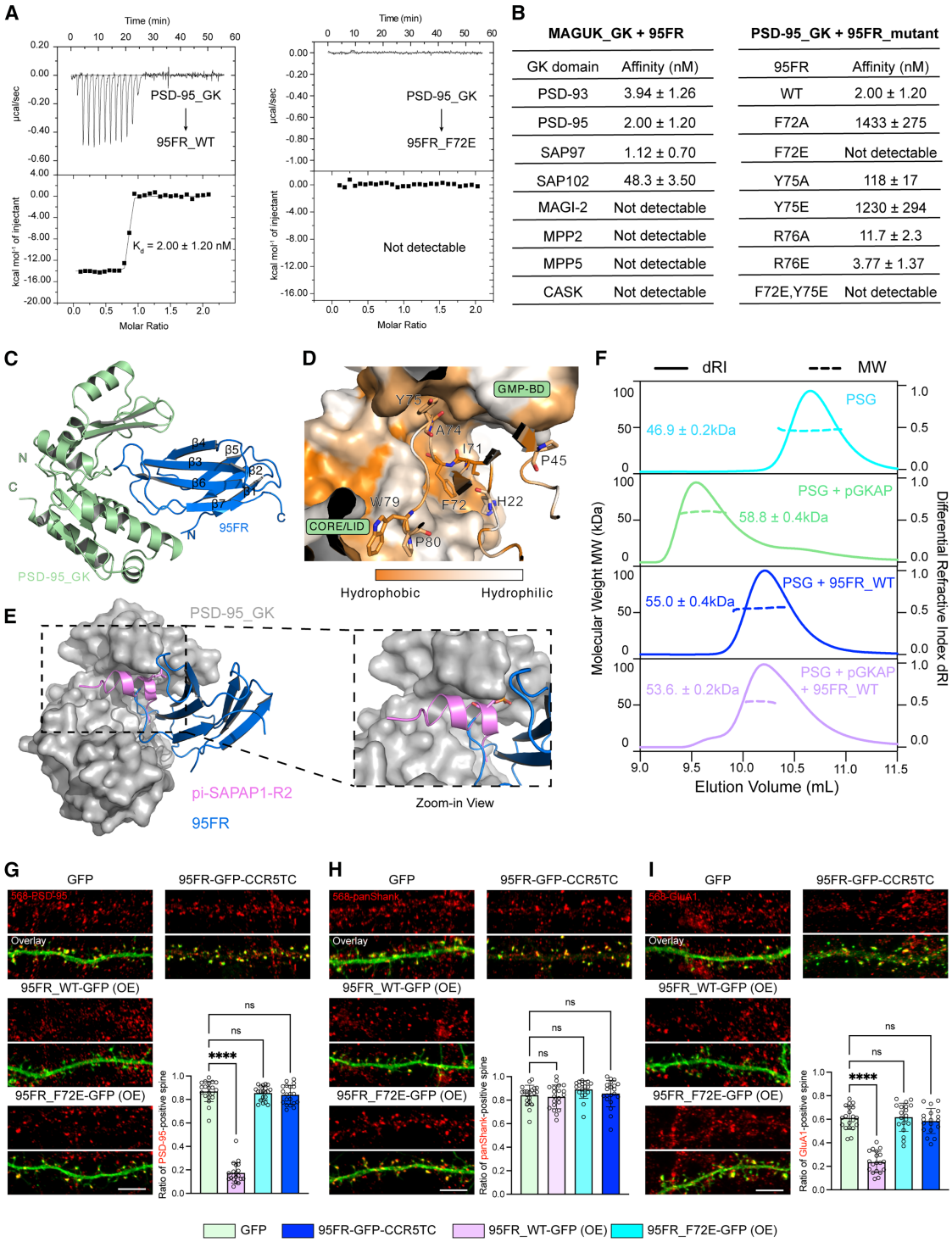


**Figure 5. 95FR specifically binds to the PSD-95 GK domain and blocks PSD-95 from binding to SAPAP**

(A) ITC-based measurement of the bindings of PSD-95_GK to 95FR_WT (left) or to 95FR_F72E (right).

(B) Left: summary of ITC-derived binding affinities of 95FR_WT to GK domains of synaptic MAGUKs. Right: summary of ITC-based measurements of binding affinities of PSD-95_GK to various 95FR mutants.

(C) Ribbon representations of the overall structure of 95FR in complex with PSD-95_GK.

(D) Surface combined with ribbon representations showing the diagram of hydrophobic interactions between PSD-95_GK and 95FR.

*(legend continued on next page)*

clustering of PSD-95 and GluA1 (Figures 5G–5I), likely due to the fact that PSD-95 is more abundant than SAPAPs in synapses.[53,54] Thus, 95FR could be used as an effective PSD-95 (or the DLG MAGUKs) labeling tool so long as the intrabody expression level is tightly controlled.

## Strengthening the PSD molecular network enhances synapse formation

We next used 95FR to strengthen the coupling of the PSD core and pallium condensates by replacing the GK-binding repeats (GBRs) of SAPAPs with 95FR (Figure 6A) and to investigate the ensuing impact on synapse formation in neurons. We first tested our design using the reconstituted PSD condensate. One GBR of recombinant SAPAP1 (a.k.a. GKAP) was replaced by 95FR_WT or 95FR_FE (Figure 6A, top). The chimeric GKAP-95FR was mixed with other four PSD proteins and the diffusion behavior of PSD core proteins was analyzed by SMT (Figures 6B, 6C, and S4G–S4J). In 5× PSD containing GKAP-95FR-WT, the mobility of Stg_CT or PSD-95 was further decreased when compared with the condensates containing GKAP-WT (Figures 6C and S4G–S4J), suggesting the enhanced PSD network stability by GKAP-95FR-WT. In contrast, mixing GKAP-95FR-FE with other PSD proteins increased the mobile ratio of Stg_CT and PSD-95 (Figures 6C and S4G–S4J).

We then verified that the full-length SAPAP3-95FR chimera could effectively couple PSD-95 and Shank3 in heterologous cells. We replaced both GBRs of full-length SAPAP3 with 95FR_WT or 95FR_F72E (Figure 6A, bottom). In HeLa cells (see Figure 6D1 for the experimental design), overexpressed GFP-Shank3 formed large puncta. Expression of SAPAP3-WT led to enrichment of expressed PSD-95 to the Shank3 puncta, whereas no enrichment could be observed if SAPAP3 was not expressed (Figures 6D and S7A). Importantly, SAPAP3-95FR expression led to a much stronger enrichment of PSD-95 to the Shank3 puncta compared with SAPAP3-WT-expressing cells (Figures 6D2 and 6D3). PSD-95 enrichments into Shank3 puncta were negligible in cells expressing SAPAP3-SA or SAPAP3-95FR-FE, both of which are defective in binding to PSD-95.[61] FRAP assay further showed that PSD-95 recruited into Shank3 puncta by SAPAP3-95FR was with much lower mobility than that recruited by SAPAP3-WT (Figures S7B–S7D). The above biochemistry and heterologous cellular data revealed that enhancing the PSD molecular network using the SAPAP-95FR chimera could enhance the PSD condensate formation and decrease the mobilities of Stg and PSD-95 in the condensate.

We then investigated whether SAPAP3-95FR could perform better than SAPAP3-WT in enhancing AMPAR clustering and synapse formation using cultured hippocampal neurons. First, using direct stochastic optical reconstruction microscopy (dSTORM)-based super-resolution imaging,[30,61] we found that expression of SAPAP3-95FR, compared with SAPAP3-WT, led to significantly enhanced co-localization of expressed SAPAP3 with endogenous PSD-95 (Figure 6E). Although SAPAP3-SA and SAPAP3-95FR-FE were localized in the dendritic spines via binding to other PSD proteins such as Shank, these two proteins showed much less overlap with PSD-95 (Figure 6E).

We then evaluated whether enhancing PSD molecular network stability would promote synaptic formation and maturation. In neurons transfected with various forms of SAPAP3 proteins, the width of the spine heads and clustering of endogenous GluA1 were quantified to evaluate the maturation of excitatory synapses. Neurons overexpressing SAPAP3-WT or SAPAP3-95FR contained larger spine heads than the GFP control or the SAPAP3 variants deficient in PSD-95_GK binding (Figure 6F). Notedly, SAPAP3-95FR promoted spine enlargement and GluA1 clustering more potently than SAPAP3-WT (Figures 6F and 6G). Taken together, the above results revealed that strengthening (or weakening) the connection between the PSD core and pallium led to enhanced (or destabilized) PSD molecular network formation and stronger (or weaker) synapses.

## Pre- and postsynaptic nanocluster modulation via manipulating the PSD molecular network

The presynaptic active zone (AZ) and the PSD of each synapse are aligned forming transsynaptic nanocolumns.[48,62,63] Mechanistically, AZ condensates and PSD condensates are bridged by various adhesion molecules in the synaptic cleft, forming transsynaptic mega-condensates.[64–66] We asked whether modulations on the postsynaptic network might alter presynaptic AZ organization. To test this, we monitored synaptic organizations by imaging the AZ protein RIM1 and PSD protein PSD-95 using dSTORM. In neurons expressing GFP as the control, single-molecule localizations of RIM1 and PSD-95 displayed typical disc-like structures that are aligned with each other (Figure 7A). Upon expression of DLS-PBM, PSD-95 signals became sparse (Figures 7A, 7D, and 7E), indicating that PSD-95 was dispersed from synapses as shown in Figure 3. To our surprise, although the overall volume was only mildly affected, RIM1 became fragmented clusters, indicating that the presynaptic organization was also altered by changing the PSD condensate network (Figures 7A–7C). Expressing the DLS-PBM$^{d}$ peptide had no impact either on the overall volume or on the nanocluster number of PSD-95 and RIM1.

(E) Superposition of the GK structures from the PSD-95_GK/95FR complex and the PSD-95_GK/pi-SAPAP1-R2 complex (PDB: 5YPO). The zoom-in view shows the overlap of the pi-SAPAP1-R2 binding site and the 95FR β6-β7 loop binding region on PSD-95_GK.

(F) Size exclusion chromatography with multi-angle static light scattering (SEC-MALS) assays showing the disruption of PSD-95_GK/pGKAP complex by 95FR. In this experiment, 30 μM PSD-95_PSG, 30 μM pGKAP, and 90 μM 95FR_WT were mixed according to the combinations marked in the panel before loading to the column.

(G–I) Representative fluorescence imaging and quantifications showing the localizations of endogenous PSD-95 (G), pan-Shank (H), GluA1 (I) in neurons expressing GFP, 95FR_WT-GFP (OE), 95FR_F72E-GFP (OE), or 95FR_WT-CCR5TC, respectively. Scale bar: 10 μm. In (G), $n = 20$ neurons. In (H), $n = 20$ neurons for all groups except 95FR_F72E-GFP with $n = 19$. In (I), GFP, $n = 20$; 95FR_WT-CCR5TC, $n = 18$; 95FR_WT-GFP and 95FR_F72E-GFP, $n = 19$. All quantification data were collected from three independent batches. Error bars indicate ± SD. One-way ANOVA followed by Tukey's post hoc test was used. ****$p < 0.0001$. ns: not significant.

See also Figures S5 and S6.

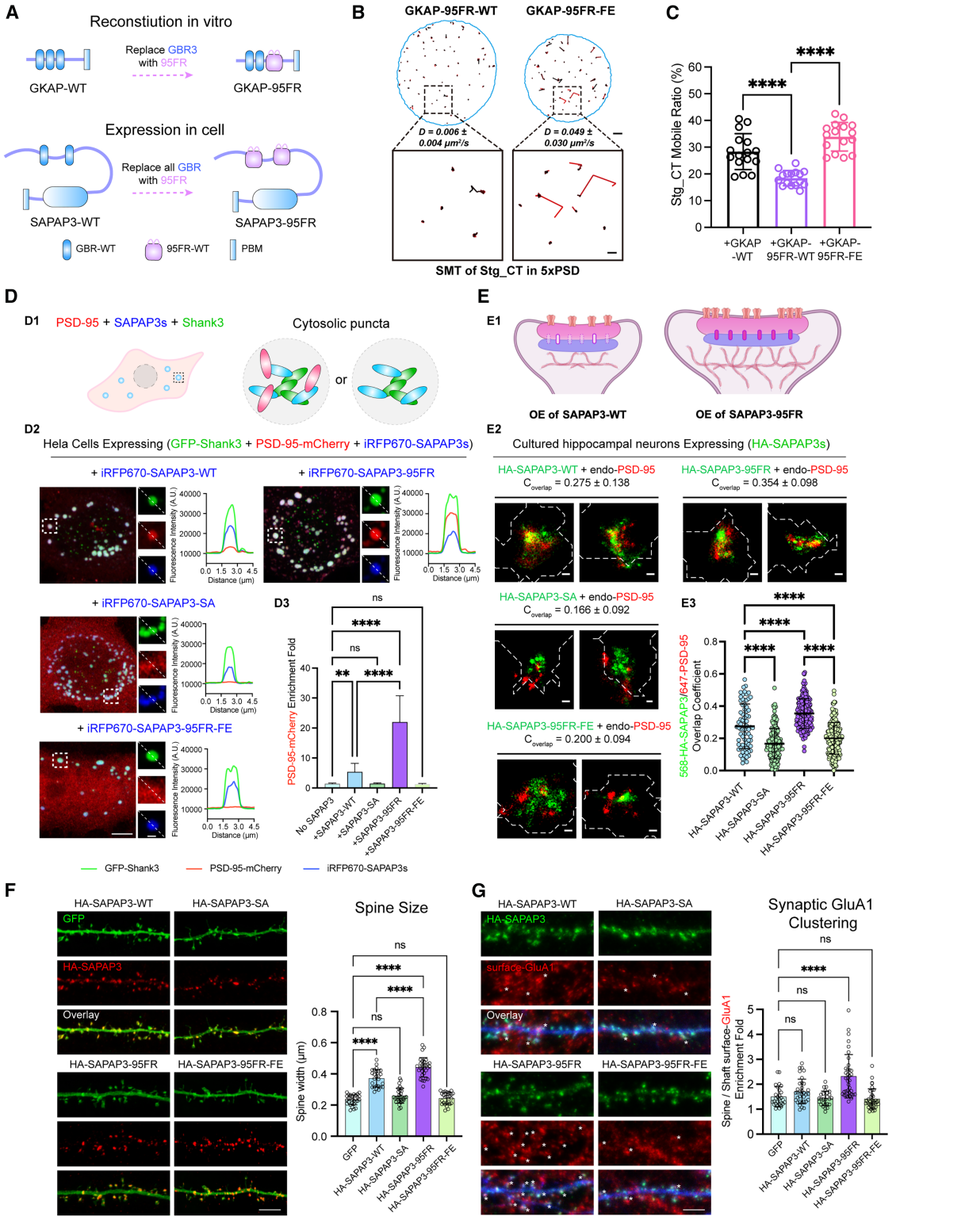


**Figure 6. Strengthening the PSD molecular network enhances synapse formation and maturation**

(A) Schematic diagram showing the design of the GKAP and SAPAP3 chimeras with enhanced bindings to PSD-95 for experiments *in vitro* and in cells described below. For the GKAP-95FR chimera, one GRB was replaced with 95FR. For the full-length SAPAP3-95FR chimera, both GBR repeats of SAPAP3 were replaced with 95FR.

*(legend continued on next page)*

Compared with neurons overexpressing SAPAP3-WT, synapses of neurons expressing SAPAP3-95FR showed decreased number of small PSD-95 and RIM1 nanoclusters (likely due to merging of small and loose nanoclusters into large and dense ones). Importantly, the ratio of the PSD-95 and RIM nanocluster volumes over the synaptic volumes were significantly increased in SAPAP3-95FR expressing neurons (i.e., both the AZ and the PSD nanoclusters in the synapses of SAPAP3-95FR expressing neurons became larger and denser) (Figures 7F–7L). These results indicate that the PSD condensate network may govern the overall organization of a synapse, which is a multi-compartment transcellular structure formed between two neurons.[67]

## DISCUSSION

Via multivalent interactions, molecular components in a biological condensate may form percolated molecular networks,[27–30] thus bringing the condensate biology to an interdisciplinary field of condensed matter physics and complex systems. The field of biological condensates is just at its beginning with many unanswered fundamental questions. For example, it is largely unknown how the network property of a biological condensate is connected to cellular functions of the condensate.

We found in this study that altering the complexity of the PSD network by specifically targeting its different interaction nodes can change the entire network and consequently alter mobilities of proteins in the condensate. Strikingly, even though the interaction between AMPAR and PSD-95 is not directly altered, blocking the PSD-95/SAPAP node or the Shank/Homer node in the PSD network caused increased receptor mobilities in synapses, causing defects in synaptic transmission and plasticity. Conversely, strengthening the PSD-95/SAPAP node with a chimeric SAPAP3-95FR protein led to a more robust network organization and further potentiates the synapse maturation process. These findings indicate that phase-separation-mediated formation of the PSD condensate renders emergent network properties for the PSD molecular assemblies. The network properties can even pass from the post-synapse in one neuron to the pre-synapse in another (Figure 7).

The concept that the entire network property is intimately linked to the mobility and hence cellular functions of each individual molecule in a biological condensate has important implications in understanding condensate biology and pathophysiology in general. Taking the PSD condensate as an example, distinct synaptic regulatory signals can act on different network nodes, and these signals can converge on the AMPAR synaptic clustering via the percolated molecular network. For instance, phosphorylation of SAPAP can enhance the PSD-95/SAPAP node and consequently promote AMPAR synaptic clustering and synaptic transmission.[37,61] Homer1a can modulate the Shank/Homer node to regulate PSD network complexity and AMPAR-mediated synaptic plasticity.[57,58,68] Arc can target the TARP/PSD-95 node to modulate the PSD network and the AMPAR synaptic functions.[5,69] Thus, the entire PSD scaffold network can function as an integrated synaptic signaling hub via formation of the PSD condensate. From the clinical perspective, mutations of many PSD proteins are implicated in neurodevelopmental diseases and psychiatric disorders.[70–72] Targeting individual PSD protein for therapeutic purposes has low applicability and high costs, as mutations of each PSD protein-encoding gene only account for a very small proportion of patients. Since the functions of numerous PSD proteins converge on the PSD network, modulating the network property might be a more effective strategy for developing therapeutics applicable for larger proportions of patients with different genotypes.

(B) Representative images showing the trajectories of Stg_CT (Cy3 labeling ratio of 0.035%) from 5× PSD condensates containing 10 μM GKAP-95FR-WT (left) or 10 μM GKAP-95FR-FE (right). Zoom-in images are used to show examples of single-molecule trajectories. The derived average apparent diffusion coefficient of each group is marked above the zoom-in images as mean ± SD. Scale bar: 1 μm (up), 250 nm (bottom).

(C) Quantification of the mobile ratios of Stg_CT in the three types of condensates based on single-molecule trajectories from (B) and Figure 4C. Error bar indicates ± SD. $n$ = 16 droplets for all groups. One-way ANOVA followed by Tukey's post hoc test, ****$p < 0.0001$.

(D) (D1) Experimental design for evaluating the targeting of PSD-95 (red) to the Shank3 puncta (green) via binding to SAPAP3 (blue) in heterologous cells. (D2) Fluorescence imaging showing the localization of PSD-95-mCherry, iRFP670-SAPAP3 variants, and GFP-Shank3 in transfected HeLa cells. The dashed boxes indicate the puncta selected for zoom-in view and line-scanning analysis. (D3) Quantification showing the enrichments of PSD-95 into the Shank3 puncta in cells expressing different SAPAP3 variants. $n$ = 28–30 cells for each group. Data were collected from two independent batches of cultures. Error bars indicate ± SD. One-way ANOVA followed by Tukey's post hoc test was used. ****$p < 0.0001$. **$p < 0.01$. ns: not significant. Scale bar: 5 μm for the large images and 1 μm for the zoom-in views.

(E) (E1) Experimental scheme showing that SAPAP3-95FR overexpression is expected to better enhance synapse formation than SAPAP3-WT in cultured hippocampal neurons. (E2) dSTORM super-resolution imaging analysis showing distributions of each exogenously expressed HA-tagged SAPAP3 variants (green dots) with respect to endogenous PSD-95 (red dots) in cultured rat hippocampal pyramidal neurons. White dashed lines demarcate the synaptic boundaries generated from the GFP signal acquired by conventional confocal imaging. Calculated overlap coefficient for each group is marked at the top of each sub-panel and expressed as average ± SD. Scale bar: 100 nm. (E3) Quantification of the super-resolution imagining experiments. The overlap coefficients were used to measure the degrees of overlaps between PSD-95 and each HA-SAPAP3 variants. The datasets (from left to right) were obtained from 72, 154, 201, 161 spines from 6 neurons in two different batches of cultures.

(F) Representative fluorescence images showing dendritic spines in hippocampal neurons expressing SAPAP3-WT, SAPAP3-SA, SAPAP3-95FR, or SAPAP3-95FR-FE. Right panel shows the quantification of spine head width of the experimental groups shown in left panel. $N$ = 29/26/30/30/27 for GFP/SAPAP3-WT/SAPAP3-SA/SAPAP3-95FR/SAPAP3-95FR-FE, respectively.

(G) Representative fluorescence images showing the localization of surface GluA1 in dendritic spines expressing SAPAP3-WT, SAPAP3-SA, SAPAP3-95FR, or SAPAP3-95FR-FE. White asterisk indicates spines with enriched GluA1 signal. Right panel is the quantification of surface GluA1 enrichment fold in spines versus shafts of the experimental groups shown in left panel. $n$ = 28/34/26/37/35 for GFP/SAPAP3-WT/SAPAP3-SA/SAPAP3-95FR/SAPAP3-95FR-FE, respectively.

For (E), (F), and (G), all datasets were collected from two independent batches. Error bars indicate ± SD. One-way ANOVA followed by Tukey's post hoc test was used. ****$p < 0.0001$. ns: not significant. Scale bar: 10 μm.

See also Figures S4 and S7. The scheme of (A) and (E1) was drawn using BioRender (https://www.biorender.com).

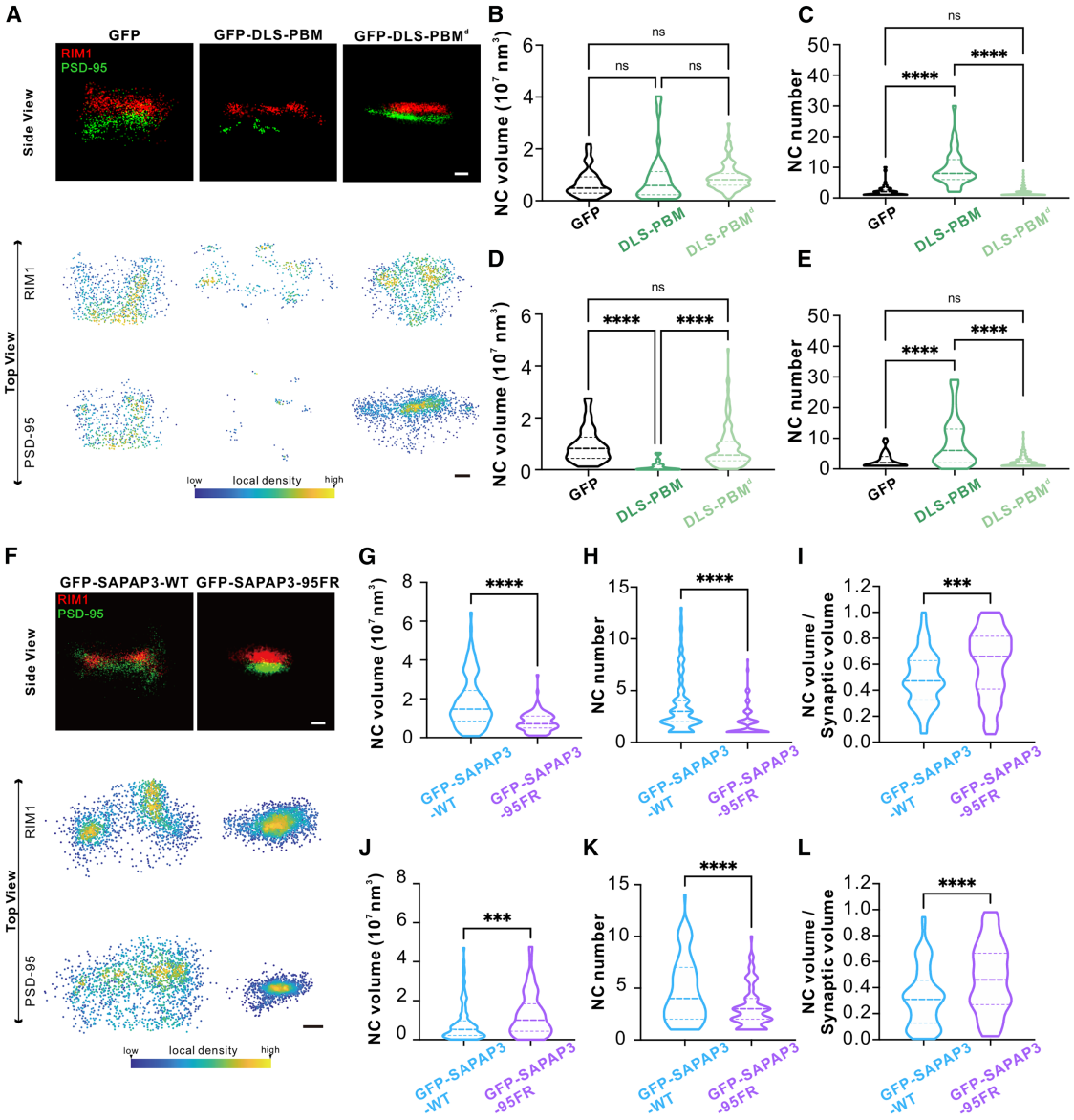


**Figure 7. Both pre- and postsynaptic nanoclusters can be modulated via manipulating the PSD molecular network**

(A) Representative dSTORM images showing the side and top views of the distributions of presynaptic AZ scaffold protein RIM1 (red) and PSD scaffold protein PSD-95 (green) in synapses expressing GFP, GFP-DLS-PBM, or GFP-DLS-PBM$^{d}$. Scale bar: 100 nm.

(B and C) Quantitative analysis of presynaptic nanocluster volumes (B) and nanocluster (NC) number (C) marked by AZ scaffold RIM1 from cultured neurons expressing GFP, GFP-DLS-PBM, or GFP-DLS-PBM$^{d}$.

(D and E) Quantitative analysis of postsynaptic nanocluster volumes (D) and nanocluster number (E) marked by PSD scaffold PSD-95 from cultured neurons expressing GFP, GFP-DLS-PBM, or GFP-DLS-PBM$^{d}$.

(F) Representative dSTORM images showing the side and top views of the distributions of presynaptic AZ scaffold protein RIM1 (red) and PSD scaffold protein PSD-95 (green) in synapses expressing GFP-SAPAP3-WT or GFP-SAPAP3-95FR. Scale bar: 100 nm.

(G–I) Quantitative analysis of the presynaptic nanocluster volumes (G), nanocluster number (H), and ratio of nanocluster volume versus synaptic volume (I) marked by AZ scaffold RIM1 from cultured neurons expressing GFP-SAPAP3-WT or GFP-SAPAP3-95FR.

(J–L) Quantitative analysis of the postsynaptic nanocluster volumes (J), nanocluster number (K), and ratio of nanocluster volume versus synaptic volume (L) marked by PSD-95 from cultured neurons expressing GFP-SAPAP3-WT or GFP-SAPAP3-95FR.

In (B)–(E), $N$ = 45,37,128 synapses from 12, 13, 12 neurons from two independent batches. One-way ANOVA followed by Tukey's post hoc test, ****$p < 0.0001$, n.s., not significant. In (G)–(L), $N$ = 126,112 synapses from 12, 10 neurons from two independent batches. Unpaired t test, ***$p < 0.001$, ****$p < 0.0001$.

**Table 1. Crystallographic data collection and refinement statistics**

| Data collection | PSD-95_GK/FingR |
|---|---|
| Space group | $P2_12_12_1$ |
| Wavelength (Å) | 0.97930 |
| Unit cell parameters a, b, c (Å) α, β, γ (°) | 66.429, 74.987, 136.567, 90 |
| Resolution range (Å) | 50–1.93 (2.04–1.93) |
| No. of unique reflections | 51,565 (7,776) |
| Redundancy | 13.1 (12.3) |
| I/σ | 12.82 (1.05) |
| Completeness (%) | 98.7 (93.6) |
| $R_{merge}$[a] (%) | 13.8 (240.2) |
| $CC_{1/2}$ | 0.999 (0.696) |
| **Structure refinement** | |
| Resolution (Å) | 1.93 |
| $R_{work}$[b] (%) | 23.87 |
| $R_{free}$[c] (%) | 27.82 |
| RMSD bonds (Å) | 0.005 |
| RMSD angles (°) | 0.766 |
| Average B factor (Å$^2$) | 53.30 |
| **No. of atoms** | |
| Protein | 4,396 |
| Ligand/ion | 32 |
| Water | 239 |
| **B factors (Å$^2$)** | |
| Proteins | 53.43 |
| Ligand/ion | 58.14 |
| Water | 50.38 |
| **Ramachandran plot (%)** | |
| Preferred | 97.76 |
| Allowed | 2.05 |
| Outliers | 0.19 |

[a]$R_{merge} = \Sigma|I_i - <I>|/\Sigma I_i$. $I_i$, intensity of measured reflection; <I>, mean intensity of all reflections.
[b]$R_{work} = \Sigma_W||F_{calc}| - |F_{obs}||/\Sigma|F_{obs}|$. $F_{obs}$ and $F_{calc}$, observed and calculated structure factors. W, working dataset of 95% of randomly chosen total reflections.
[c]$R_{free} = \Sigma_T||F_{calc}| - |F_{obs}||/\Sigma|F_{obs}|$. T, test dataset of the remaining 5% total reflections.

## Limitations of the study

Extensive studies using soft-mater physics methods[31] and single-molecule tracking technology[27,30] revealed that scaffold proteins in the PSD condensate formed dynamically and non-covalently cross-linked molecular network, resulting in coexistence of and exchange between confined molecular components on the network and mobile proteins off the network. These studies revealed that the molecular network within the PSD condensate has a slow power-law relaxation behavior at a length scale much larger than the hydrodynamic radius of each protein,[31] thus indicating that the PSD molecular network is system-spanning (i.e., percolated). However, directly visualizing a percolated molecular network at the individual protein level has not been made possible. The concept of the percolated PSD condensate molecular network described in this work and in our previous works is inferred instead of directly visualized, and this is a key limitation of the current study.

Directly proving PSD formation via phase separation in synapses of living neurons is extremely challenging as the sizes of synapses are near the diffraction limit of optical microscopes. As an alternative, we have combined *in vitro* reconstituted PSD condensates and super-resolution imaging approaches in living neurons to study phase separation-mediated formation and regulation of the dynamic PSD molecular network.

## RESOURCE AVAILABILITY

### Lead contact

Further information and requests for resources should be directed to and will be fulfilled by the lead contact, Mingjie Zhang (zhangmj@sustech.edu.cn).

### Materials availability

This study did not generate new unique reagents.

### Data and code availability

- The atomic coordinates of the PSD-95_GK and PSD-95.FingR complex can be accessed at the Protein Data Bank with the accession number 9IUI.
- Any additional information required to reanalyze the data reported in this paper is available from the lead contact upon request.
- Original code is available at Github (https://github.com/NeoLShen/Code-for-phase-simulation-and-HMM-analysis).

## ACKNOWLEDGMENTS

This work was supported by grants from the National Natural Science Foundation of China (82188101 and 32494762), Shenzhen Talent Program (KQTD20210811090115021), Shenzhen Science and Technology Basic Research Program (JCYJ20220818100215033), Guangdong Innovative and Entrepreneurial Research Team Program (2021ZT09Y104), Shenzhen Medical Research Fund (B2302039), and Key-Area Research and Development Program of Guangdong Province (2023B0303010001) to M.Z., National Natural Science Foundation of China (31721002, 81920208014, 31930051 to Y.L., and 32200795 to H.L.); Natural Science Foundation of Hubei Province (2022CFB608) to H.L. We thank the Biosciences Central Research Facility at HKUST for the super-resolution imaging microscopy and the BL19U1 beamline at National Facility for Protein Science Shanghai (NFPS) for X-ray beam time.

## AUTHOR CONTRIBUTIONS

B.J., S. Zhu, Z.S., and M.Z. conceived the idea and designed the experiments; B.J. and S. Zhu performed all biochemical and cell biology experiments with helps from Y.W.; Z.S. performed single molecule tracking and super-resolution imaging experiments with helps from S. Zhu and Z.W.; Q.C. determined the structure of the PSD-95_GK/95FR complex; X.C. performed electrophysiology experiments, H.L. and S. Zhao performed the mouse behavior experiments; all authors analyzed the results. B.J., S. Zhu, Z.S., and M.Z. wrote the manuscript with input from other authors. R.A.N., Y.L., and M.Z. supervised the research. M.Z. coordinated the project.

## DECLARATION OF INTERESTS

The authors declare no competing interests.

## STAR★METHODS

Detailed methods are provided in the online version of this paper and include the following:

- KEY RESOURCES TABLE
- EXPERIMENTAL MODEL AND STUDY PARTICIPANT DETAILS
  - Bacterial Strain
  - Cell line
- METHOD DETAILS
  - DNA constructs and chemical agents
  - Protein expression and purification
  - Isothermal titration calorimetry assay
  - Size exclusion chromatography coupled with multi-angle light scattering (SEC-MALS) assay
  - Protein crystallization and structure determination
  - AAV preparation
  - Slice culture and transfection
  - Acute slice preparation
  - Electrophysiological recording
  - Behavioral analyses
  - Primary hippocampal neuron culture
  - HeLa cell culture
  - Immunocytochemistry
  - PSD preparation
  - Fluorescence recovery after photobleaching (FRAP) assay
  - Protein fluorescence labeling
  - In vitro GKAP/SAPAP1 phosphorylation
  - Imaging-based assay of phase separation
  - Single molecule tracking assay
  - 3D dSTORM imaging
  - Quantification of dSTORM imaging for cultured neuron
- QUANTIFICATION AND STATISTICAL ANALYSIS

## SUPPLEMENTAL INFORMATION

Supplemental information can be found online at https://doi.org/10.1016/j.molcel.2025.07.017.

Received: October 13, 2024
Revised: May 27, 2025
Accepted: July 25, 2025
Published: August 12, 2025

## REFERENCES

1. Boeynaems, S., Alberti, S., Fawzi, N.L., Mittag, T., Polymenidou, M., Rousseau, F., Schymkowitz, J., Shorter, J., Wolozin, B., Van Den Bosch, L., et al. (2018). Protein Phase Separation: A New Phase in Cell Biology. Trends Cell Biol. *28*, 420–435. https://doi.org/10.1016/j.tcb.2018.02.004.
2. Brangwynne, C.P., Eckmann, C.R., Courson, D.S., Rybarska, A., Hoege, C., Gharakhani, J., Jülicher, F., and Hyman, A.A. (2009). Germline P granules are liquid droplets that localize by controlled dissolution/condensation. Science *324*, 1729–1732. https://doi.org/10.1126/science.1172046.
3. Shin, Y., and Brangwynne, C.P. (2017). Liquid phase condensation in cell physiology and disease. Science *357*, eaaf4382. https://doi.org/10.1126/science.aaf4382.
4. Banani, S.F., Lee, H.O., Hyman, A.A., and Rosen, M.K. (2017). Biomolecular condensates: organizers of cellular biochemistry. Nat. Rev. Mol. Cell Biol. *18*, 285–298. https://doi.org/10.1038/nrm.2017.7.
5. Chen, X., Jia, B., Araki, Y., Liu, B., Ye, F., Huganir, R., and Zhang, M. (2022). Arc weakens synapses by dispersing AMPA receptors from postsynaptic density via modulating PSD phase separation. Cell Res. *32*, 914–930. https://doi.org/10.1038/s41422-022-00697-9.
6. Wu, X., Ganzella, M., Zhou, J., Zhu, S., Jahn, R., and Zhang, M. (2021). Vesicle Tethering on the Surface of Phase-Separated Active Zone Condensates. Mol. Cell *81*, 13–24.e7. https://doi.org/10.1016/j.molcel.2020.10.029.
7. Zeng, M., Chen, X., Guan, D., Xu, J., Wu, H., Tong, P., and Zhang, M. (2018). Reconstituted Postsynaptic Density as a Molecular Platform for Understanding Synapse Formation and Plasticity. Cell *174*, 1172–1187. e16. https://doi.org/10.1016/j.cell.2018.06.047.
8. Protter, D.S.W., and Parker, R. (2016). Principles and Properties of Stress Granules. Trends Cell Biol. *26*, 668–679. https://doi.org/10.1016/j.tcb.2016.05.004.
9. Patel, A., Lee, H.O., Jawerth, L., Maharana, S., Jahnel, M., Hein, M.Y., Stoynov, S., Mahamid, J., Saha, S., Franzmann, T.M., et al. (2015). A Liquid-to-Solid Phase Transition of the ALS Protein FUS Accelerated by Disease Mutation. Cell *162*, 1066–1077. https://doi.org/10.1016/j.cell.2015.07.047.
10. Marcelo, A., Koppenol, R., de Almeida, L.P., Matos, C.A., and Nóbrega, C. (2021). Stress granules, RNA-binding proteins and polyglutamine diseases: too much aggregation? Cell Death Dis. *12*, 592. https://doi.org/10.1038/s41419-021-03873-8.
11. Guillén-Boixet, J., Kopach, A., Holehouse, A.S., Wittmann, S., Jahnel, M., Schlüßler, R., Kim, K., Trussina, I.R.E.A., Wang, J., Mateju, D., et al. (2020). RNA-Induced Conformational Switching and Clustering of G3BP Drive Stress Granule Assembly by Condensation. Cell *181*, 346–361.e17. https://doi.org/10.1016/j.cell.2020.03.049.
12. Xiao, Q., McAtee, C.K., and Su, X. (2022). Phase separation in immune signalling. Nat. Rev. Immunol. *22*, 188–199. https://doi.org/10.1038/s41577-021-00572-5.
13. Su, X., Ditlev, J.A., Hui, E., Xing, W., Banjade, S., Okrut, J., King, D.S., Taunton, J., Rosen, M.K., and Vale, R.D. (2016). Phase separation of signaling molecules promotes T cell receptor signal transduction. Science *352*, 595–599. https://doi.org/10.1126/science.aad9964.
14. Du, M., and Chen, Z.J. (2018). DNA-induced liquid phase condensation of cGAS activates innate immune signaling. Science *361*, 704–709. https://doi.org/10.1126/science.aat1022.
15. Zhang, X., Bai, X.C., and Chen, Z.J. (2020). Structures and Mechanisms in the cGAS-STING Innate Immunity Pathway. Immunity *53*, 43–53. https://doi.org/10.1016/j.immuni.2020.05.013.
16. Shan, L., Xu, G., Yao, R.W., Luan, P.F., Huang, Y., Zhang, P.H., Pan, Y.H., Zhang, L., Gao, X., Li, Y., et al. (2023). Nucleolar URB1 ensures 3′ ETS rRNA removal to prevent exosome surveillance. Nature *615*, 526–534. https://doi.org/10.1038/s41586-023-05767-5.
17. Feric, M., Vaidya, N., Harmon, T.S., Mitrea, D.M., Zhu, L., Richardson, T.M., Kriwacki, R.W., Pappu, R.V., and Brangwynne, C.P. (2016). Coexisting Liquid Phases Underlie Nucleolar Subcompartments. Cell *165*, 1686–1697. https://doi.org/10.1016/j.cell.2016.04.047.
18. Lafontaine, D.L.J., Riback, J.A., Bascetin, R., and Brangwynne, C.P. (2021). The nucleolus as a multiphase liquid condensate. Nat. Rev. Mol. Cell Biol. *22*, 165–182. https://doi.org/10.1038/s41580-020-0272-6.
19. Ukmar-Godec, T., Cima-Omori, M.S., Yerkesh, Z., Eswara, K., Yu, T., Ramesh, R., Riviere, G., Ibanez de Opakua, A., Fischle, W., and Zweckstetter, M. (2023). Multimodal interactions drive chromatin phase separation and compaction. Proc. Natl. Acad. Sci. USA *120*, e2308858120. https://doi.org/10.1073/pnas.2308858120.
20. Gibson, B.A., Doolittle, L.K., Schneider, M.W.G., Jensen, L.E., Gamarra, N., Henry, L., Gerlich, D.W., Redding, S., and Rosen, M.K. (2019). Organization of Chromatin by Intrinsic and Regulated Phase Separation. Cell *179*, 470–484.e21. https://doi.org/10.1016/j.cell.2019.08.037.
21. Strom, A.R., Emelyanov, A.V., Mir, M., Fyodorov, D.V., Darzacq, X., and Karpen, G.H. (2017). Phase separation drives heterochromatin domain formation. Nature *547*, 241–245. https://doi.org/10.1038/nature22989.
22. Mensah, M.A., Niskanen, H., Magalhaes, A.P., Basu, S., Kircher, M., Sczakiel, H.L., Reiter, A.M.V., Elsner, J., Meinecke, P., Biskup, S., et al. (2023). Aberrant phase separation and nucleolar dysfunction in rare

genetic diseases. Nature *614*, 564–571. https://doi.org/10.1038/s41586-022-05682-1.

23. Tong, X., Tang, R., Xu, J., Wang, W., Zhao, Y., Yu, X., and Shi, S. (2022). Liquid-liquid phase separation in tumor biology. Signal Transduct. Target. Ther. *7*, 221. https://doi.org/10.1038/s41392-022-01076-x.
24. Zbinden, A., Pérez-Berlanga, M., De Rossi, P., and Polymenidou, M. (2020). Phase Separation and Neurodegenerative Diseases: A Disturbance in the Force. Dev. Cell *55*, 45–68. https://doi.org/10.1016/j.devcel.2020.09.014.
25. Wang, L., and Zhou, W. (2024). Phase separation as a new form of regulation in innate immunity. Mol. Cell *84*, 2410–2422. https://doi.org/10.1016/j.molcel.2024.06.004.
26. So, C., Cheng, S., and Schuh, M. (2021). Phase Separation during Germline Development. Trends Cell Biol. *31*, 254–268. https://doi.org/10.1016/j.tcb.2020.12.004.
27. Shen, Z., Jia, B., Xu, Y., Wessén, J., Pal, T., Chan, H.S., Du, S., and Zhang, M. (2023). Biological condensates form percolated networks with molecular motion properties distinctly different from dilute solutions. eLife *12*, e81907. https://doi.org/10.7554/eLife.81907.
28. Li, P., Banjade, S., Cheng, H.C., Kim, S., Chen, B., Guo, L., Llaguno, M., Hollingsworth, J.V., King, D.S., Banani, S.F., et al. (2012). Phase transitions in the assembly of multivalent signalling proteins. Nature *483*, 336–340. https://doi.org/10.1038/nature10879.
29. Mittag, T., and Pappu, R.V. (2022). A conceptual framework for understanding phase separation and addressing open questions and challenges. Mol. Cell *82*, 2201–2214. https://doi.org/10.1016/j.molcel.2022.05.018.
30. Zhu, S., Shen, Z., Wu, X., Han, W., Jia, B., Lu, W., and Zhang, M. (2024). Demixing is a default process for biological condensates formed via phase separation. Science *384*, 920–928. https://doi.org/10.1126/science.adj7066.
31. Liao, Z., Jia, B., Guan, D., Chen, X., Zhang, M., and Tong, P. (2025). Emergent mechanics of a networked multivalent protein condensate. Nat. Commun. *16*, 5237. https://doi.org/10.1038/s41467-025-60345-9.
32. Matsuzaki, M., Honkura, N., Ellis-Davies, G.C.R., and Kasai, H. (2004). Structural basis of long-term potentiation in single dendritic spines. Nature *429*, 761–766. https://doi.org/10.1038/nature02617.
33. Kasai, H., Matsuzaki, M., Noguchi, J., Yasumatsu, N., and Nakahara, H. (2003). Structure-stability-function relationships of dendritic spines. Trends Neurosci. *26*, 360–368. https://doi.org/10.1016/S0166-2236(03)00162-0.
34. Holler, S., Köstinger, G., Martin, K.A.C., Schuhknecht, G.F.P., and Stratford, K.J. (2021). Structure and function of a neocortical synapse. Nature *591*, 111–116. https://doi.org/10.1038/s41586-020-03134-2.
35. Zhu, J., Shang, Y., and Zhang, M. (2016). Mechanistic basis of MAGUK-organized complexes in synaptic development and signalling. Nat. Rev. Neurosci. *17*, 209–223. https://doi.org/10.1038/nrn.2016.18.
36. Bosch, M., Castro, J., Saneyoshi, T., Matsuno, H., Sur, M., and Hayashi, Y. (2014). Structural and molecular remodeling of dendritic spine substructures during long-term potentiation. Neuron *82*, 444–459. https://doi.org/10.1016/j.neuron.2014.03.021.
37. Zhu, J., Zhou, Q., Shang, Y., Li, H., Peng, M., Ke, X., Weng, Z., Zhang, R., Huang, X., Li, S.S.C., et al. (2017). Synaptic Targeting and Function of SAPAPs Mediated by Phosphorylation-Dependent Binding to PSD-95 MAGUKs. Cell Rep. *21*, 3781–3793. https://doi.org/10.1016/j.celrep.2017.11.107.
38. Zeng, M., Ye, F., Xu, J., and Zhang, M. (2018). PDZ Ligand Binding-Induced Conformational Coupling of the PDZ-SH3-GK Tandems in PSD-95 Family MAGUKs. J. Mol. Biol. *430*, 69–86. https://doi.org/10.1016/j.jmb.2017.11.003.
39. Saro, D., Li, T., Rupasinghe, C., Paredes, A., Caspers, N., and Spaller, M. R. (2007). A thermodynamic ligand binding study of the third PDZ domain (PDZ3) from the mammalian neuronal protein PSD-95. Biochemistry *46*, 6340–6352. https://doi.org/10.1021/bi062088k.
40. Zhu, J., Shang, Y., Xia, C., Wang, W., Wen, W., and Zhang, M. (2011). Guanylate kinase domains of the MAGUK family scaffold proteins as specific phospho-protein-binding modules. EMBO J. *30*, 4986–4997. https://doi.org/10.1038/emboj.2011.428.
41. Laursen, L., Karlsson, E., Gianni, S., and Jemth, P. (2020). Functional interplay between protein domains in a supramodular structure involving the postsynaptic density protein PSD-95. J. Biol. Chem. *295*, 1992–2000. https://doi.org/10.1074/jbc.RA119.011050.
42. Li, Y., Wei, Z., Yan, Y., Wan, Q., Du, Q., and Zhang, M. (2014). Structure of Crumbs tail in complex with the PALS1 PDZ-SH3-GK tandem reveals a highly specific assembly mechanism for the apical Crumbs complex. Proc. Natl. Acad. Sci. USA *111*, 17444–17449. https://doi.org/10.1073/pnas.1416515111.
43. Jumper, J., Evans, R., Pritzel, A., Green, T., Figurnov, M., Ronneberger, O., Tunyasuvunakool, K., Bates, R., Žídek, A., Potapenko, A., et al. (2021). Highly accurate protein structure prediction with AlphaFold. Nature *596*, 583–589. https://doi.org/10.1038/s41586-021-03819-2.
44. Danielson, E., Zhang, N., Metallo, J., Kaleka, K., Shin, S.M., Gerges, N., and Lee, S.H. (2012). S-SCAM/MAGI-2 is an essential synaptic scaffolding molecule for the GluA2-containing maintenance pool of AMPA receptors. J. Neurosci. *32*, 6967–6980. https://doi.org/10.1523/JNEUROSCI.0025-12.2012.
45. Nair, D., Hosy, E., Petersen, J.D., Constals, A., Giannone, G., Choquet, D., and Sibarita, J.B. (2013). Super-resolution imaging reveals that AMPA receptors inside synapses are dynamically organized in nanodomains regulated by PSD95. J. Neurosci. *33*, 13204–13224. https://doi.org/10.1523/JNEUROSCI.2381-12.2013.
46. Zeng, M., Díaz-Alonso, J., Ye, F., Chen, X., Xu, J., Ji, Z., Nicoll, R.A., and Zhang, M. (2019). Phase Separation-Mediated TARP/MAGUK Complex Condensation and AMPA Receptor Synaptic Transmission. Neuron *104*, 529–543.e6. https://doi.org/10.1016/j.neuron.2019.08.001.
47. Dosemeci, A., Weinberg, R.J., Reese, T.S., and Tao-Cheng, J.H. (2016). The Postsynaptic Density: There Is More than Meets the Eye. Front. Synaptic Neurosci. *8*, 23. https://doi.org/10.3389/fnsyn.2016.00023.
48. Dani, A., Huang, B., Bergan, J., Dulac, C., and Zhuang, X. (2010). Superresolution imaging of chemical synapses in the brain. Neuron *68*, 843–856. https://doi.org/10.1016/j.neuron.2010.11.021.
49. Hayashi, M.K., Tang, C., Verpelli, C., Narayanan, R., Stearns, M.H., Xu, R. M., Li, H., Sala, C., and Hayashi, Y. (2009). The postsynaptic density proteins Homer and Shank form a polymeric network structure. Cell *137*, 159–171. https://doi.org/10.1016/j.cell.2009.01.050.
50. Chen, X., Jia, B., Zhu, S., and Zhang, M. (2023). Phase separation-mediated actin bundling by the postsynaptic density condensates. eLife *12*, e84446. https://doi.org/10.7554/eLife.84446.
51. Hruska, M., Henderson, N.T., Xia, N.L., Le Marchand, S.J., and Dalva, M. B. (2015). Anchoring and synaptic stability of PSD-95 is driven by ephrin-B3. Nat. Neurosci. *18*, 1594–1605. https://doi.org/10.1038/nn.4140.
52. Fukata, Y., Dimitrov, A., Boncompain, G., Vielemeyer, O., Perez, F., and Fukata, M. (2013). Local palmitoylation cycles define activity-regulated postsynaptic subdomains. J. Cell Biol. *202*, 145–161. https://doi.org/10.1083/jcb.201302071.
53. Cheng, D., Hoogenraad, C.C., Rush, J., Ramm, E., Schlager, M.A., Duong, D.M., Xu, P., Wijayawardana, S.R., Hanfelt, J., Nakagawa, T., et al. (2006). Relative and absolute quantification of postsynaptic density proteome isolated from rat forebrain and cerebellum. Mol. Cell. Proteomics *5*, 1158–1170. https://doi.org/10.1074/mcp.D500009-MCP200.
54. Sheng, M., and Kim, E. (2011). The postsynaptic organization of synapses. Cold Spring Harb. Perspect. Biol. *3*, a005678. https://doi.org/10.1101/cshperspect.a005678.
55. Araki, Y., Zeng, M., Zhang, M., and Huganir, R.L. (2015). Rapid dispersion of SynGAP from synaptic spines triggers AMPA receptor insertion and

spine enlargement during LTP. Neuron *85*, 173–189. https://doi.org/10.1016/j.neuron.2014.12.023.

56. Gamache, T.R., Araki, Y., and Huganir, R.L. (2020). Twenty Years of SynGAP Research: From Synapses to Cognition. J. Neurosci. *40*, 1596–1605. https://doi.org/10.1523/JNEUROSCI.0420-19.2020.

57. Diering, G.H., Nirujogi, R.S., Roth, R.H., Worley, P.F., Pandey, A., and Huganir, R.L. (2017). Homer1a drives homeostatic scaling-down of excitatory synapses during sleep. Science *355*, 511–515. https://doi.org/10.1126/science.aai8355.

58. Sala, C., Futai, K., Yamamoto, K., Worley, P.F., Hayashi, Y., and Sheng, M. (2003). Inhibition of dendritic spine morphogenesis and synaptic transmission by activity-inducible protein Homer1a. J. Neurosci. *23*, 6327–6337. https://doi.org/10.1523/JNEUROSCI.23-15-06327.2003.

59. Hayashi, M.K., Ames, H.M., and Hayashi, Y. (2006). Tetrameric hub structure of postsynaptic scaffolding protein homer. J. Neurosci. *26*, 8492–8501. https://doi.org/10.1523/JNEUROSCI.2731-06.2006.

60. Gross, G.G., Junge, J.A., Mora, R.J., Kwon, H.B., Olson, C.A., Takahashi, T.T., Liman, E.R., Ellis-Davies, G.C.R., McGee, A.W., Sabatini, B.L., et al. (2013). Recombinant probes for visualizing endogenous synaptic proteins in living neurons. Neuron *78*, 971–985. https://doi.org/10.1016/j.neuron.2013.04.017.

61. Wu, H., Chen, X., Shen, Z., Li, H., Liang, S., Lu, Y., and Zhang, M. (2024). Phosphorylation-dependent membraneless organelle fusion and fission illustrated by postsynaptic density assemblies. Mol. Cell *84*, 309–326.e7. https://doi.org/10.1016/j.molcel.2023.11.011.

62. Tang, A.H., Chen, H., Li, T.P., Metzbower, S.R., MacGillavry, H.D., and Blanpied, T.A. (2016). A trans-synaptic nanocolumn aligns neurotransmitter release to receptors. Nature *536*, 210–214. https://doi.org/10.1038/nature19058.

63. Südhof, T.C. (2012). The presynaptic active zone. Neuron *75*, 11–25. https://doi.org/10.1016/j.neuron.2012.06.012.

64. Chen, X., Wu, X., Wu, H., and Zhang, M. (2020). Phase separation at the synapse. Nat. Neurosci. *23*, 301–310. https://doi.org/10.1038/s41593-019-0579-9.

65. Ramsey, A.M., Tang, A.H., LeGates, T.A., Gou, X.Z., Carbone, B.E., Thompson, S.M., Biederer, T., and Blanpied, T.A. (2021). Subsynaptic positioning of AMPARs by LRRTM2 controls synaptic strength. Sci. Adv. *7*, eabf3126. https://doi.org/10.1126/sciadv.abf3126.

66. Zhang, X., Chen, X., Matúš, D., and Südhof, T.C. (2025). Reconstitution of synaptic junctions orchestrated by teneurin-latrophilin complexes. Science *387*, 322–329. https://doi.org/10.1126/science.adq3586.

67. Wu, X., Shen, Z., and Zhang, M. (2025). Phase Separation-Mediated Compartmentalization Underlies Synapse Formation and Plasticity. Annu. Rev. Neurosci. *48*, 149–168. https://doi.org/10.1146/annurev-neuro-112723-040159.

68. Rozov, A., Zivkovic, A.R., and Schwarz, M.K. (2012). Homer1 gene products orchestrate Ca(2+)-permeable AMPA receptor distribution and LTP expression. Front. Synaptic Neurosci. *4*, 4. https://doi.org/10.3389/fnsyn.2012.00004.

69. Shepherd, J.D., Rumbaugh, G., Wu, J., Chowdhury, S., Plath, N., Kuhl, D., Huganir, R.L., and Worley, P.F. (2006). Arc/Arg3.1 mediates homeostatic synaptic scaling of AMPA receptors. Neuron *52*, 475–484. https://doi.org/10.1016/j.neuron.2006.08.034.

70. Bai, Y., Wang, H., and Li, C. (2022). SAPAP Scaffold Proteins: From Synaptic Function to Neuropsychiatric Disorders. Cells *11*, 3815. https://doi.org/10.3390/cells11233815.

71. Levy, A.M., Gomez-Puertas, P., and Tümer, Z. (2022). Neurodevelopmental Disorders Associated with PSD-95 and Its Interaction Partners. Int. J. Mol. Sci. *23*, 4390. https://doi.org/10.3390/ijms23084390.

72. Monteiro, P., and Feng, G. (2017). SHANK proteins: roles at the synapse and in autism spectrum disorder. Nat. Rev. Neurosci. *18*, 147–157. https://doi.org/10.1038/nrn.2016.183.

73. Cai, Q., Zeng, M., Wu, X., Wu, H., Zhan, Y., Tian, R., and Zhang, M. (2021). CaMKIIalpha-driven, phosphatase-checked postsynaptic plasticity via phase separation. Cell Res. *31*, 37–51. https://doi.org/10.1038/s41422-020-00439-9.

74. Zhang, M., Cao, A., Lin, L., Chen, Y., Shang, Y., Wang, C., Zhang, M., and Zhu, J. (2023). Phosphorylation-dependent recognition of diverse protein targets by the cryptic GK domain of MAGI MAGUKs. Sci. Adv. *9*, eadf3295. https://doi.org/10.1126/sciadv.adf3295.

75. McCoy, A.J., Grosse-Kunstleve, R.W., Adams, P.D., Winn, M.D., Storoni, L.C., and Read, R.J. (2007). Phaser crystallographic software. J. Appl. Crystallogr. *40*, 658–674. https://doi.org/10.1107/S0021889807021206.

76. Emsley, P., Lohkamp, B., Scott, W.G., and Cowtan, K. (2010). Features and development of Coot. Acta Crystallogr. D Biol. Crystallogr. *66*, 486–501. https://doi.org/10.1107/S0907444910007493.

77. Murshudov, G.N., Skubák, P., Lebedev, A.A., Pannu, N.S., Steiner, R.A., Nicholls, R.A., Winn, M.D., Long, F., and Vagin, A.A. (2011). REFMAC5 for the refinement of macromolecular crystal structures. Acta Crystallogr. D Biol. Crystallogr. *67*, 355–367. https://doi.org/10.1107/S0907444911001314.

78. Afonine, P.V., Grosse-Kunstleve, R.W., Echols, N., Headd, J.J., Moriarty, N.W., Mustyakimov, M., Terwilliger, T.C., Urzhumtsev, A., Zwart, P.H., and Adams, P.D. (2012). Towards automated crystallographic structure refinement with phenix.refine. Acta Crystallogr. D Biol. Crystallogr. *68*, 352–367. https://doi.org/10.1107/S0907444912001308.

79. Williams, C.J., Headd, J.J., Moriarty, N.W., Prisant, M.G., Videau, L.L., Deis, L.N., Verma, V., Keedy, D.A., Hintze, B.J., Chen, V.B., et al. (2018). MolProbity: more and better reference data for improved all-atom structure validation. Protein Sci. *27*, 293–315. https://doi.org/10.1002/pro.3330.

80. Chen, V.B., Arendall, W.B., Headd, J.J., Keedy, D.A., Immormino, R.M., Kapral, G.J., Murray, L.W., Richardson, J.S., and Richardson, D.C. (2010). MolProbity: all-atom structure validation for macromolecular crystallography. Acta Crystallogr. D Biol. Crystallogr. *66*, 12–21. https://doi.org/10.1107/S0907444909042073.

81. Challis, R.C., Ravindra Kumar, S., Chan, K.Y., Challis, C., Beadle, K., Jang, M.J., Kim, H.M., Rajendran, P.S., Tompkins, J.D., Shivkumar, K., et al. (2019). Systemic AAV vectors for widespread and targeted gene delivery in rodents. Nat. Protoc. *14*, 379–414. https://doi.org/10.1038/s41596-018-0097-3.

82. Stoppini, L., Buchs, P.A., and Muller, D. (1991). A simple method for organotypic cultures of nervous tissue. J. Neurosci. Methods *37*, 173–182. https://doi.org/10.1016/0165-0270(91)90128-m.

83. Diering, G.H., Gustina, A.S., and Huganir, R.L. (2014). PKA-GluA1 coupling via AKAP5 controls AMPA receptor phosphorylation and cell-surface targeting during bidirectional homeostatic plasticity. Neuron *84*, 790–805. https://doi.org/10.1016/j.neuron.2014.09.024.

84. Levet, F., Hosy, E., Kechkar, A., Butler, C., Beghin, A., Choquet, D., and Sibarita, J.B. (2015). SR-Tesseler: a method to segment and quantify localization-based super-resolution microscopy data. Nat. Methods *12*, 1065–1071. https://doi.org/10.1038/nmeth.3579.

85. Levet, F., Julien, G., Galland, R., Butler, C., Beghin, A., Chazeau, A., Hoess, P., Ries, J., Giannone, G., and Sibarita, J.B. (2019). A tessellation-based colocalization analysis approach for single-molecule localization microscopy. Nat. Commun. *10*, 2379. https://doi.org/10.1038/s41467-019-10007-4.

86. Li, T.P., Song, Y., MacGillavry, H.D., Blanpied, T.A., and Raghavachari, S. (2016). Protein Crowding within the Postsynaptic Density Can Impede the Escape of Membrane Proteins. J. Neurosci. *36*, 4276–4295. https://doi.org/10.1523/JNEUROSCI.3154-15.2016.

## STAR★METHODS

### KEY RESOURCES TABLE

| REAGENT or RESOURCE | SOURCE | IDENTIFIER |
|---|---|---|
| **Antibodies** | | |
| Mouse monoclonal anti-PSD-95 | Millipore | Cat#MAB1596; RRID: AB_2092365 |
| Mouse monoclonal anti-GluA1 | Millipore | Cat#MAB2263; RRID: AB_11212678 |
| Mouse monoclonal anti-panShank | BioLegend | Cat#851902; RRID: AB_2728584 |
| Rabbit polyclonal anti-RIM1 | Synaptic Systems | Cat#140003; RRID: AB_887774 |
| Rabbit polyclonal anti-HA | Sigma-Aldrich | Cat#H6908; RRID: AB_260070 |
| Rabbit polyclonal anti-SynGAP | Invitrogen | Cat#PA1-046; RRID: AB_2287112 |
| Mouse monoclonal anti-beta actin | Proteintech | Cat#60008-1-Ig; RRID: AB_2289225 |
| Donkey polyclonal anti-mouse IgG (H+L), Alexa Fluor™ 568 | Invitrogen | Cat#A10037; RRID: AB_11180865 |
| Donkey polyclonal anti-mouse IgG (H+L), Alexa Fluor™ 647 | Invitrogen | Cat#A31571; RRID: AB_162542 |
| Donkey polyclonal anti-rabbit IgG (H+L), Alexa Fluor™ 488 | Invitrogen | Cat#A21206; RRID: AB_2535792 |
| Donkey polyclonal anti-rabbit IgG (H+L), Alexa Fluor™ 568 | Invitrogen | Cat#A10042; RRID: AB_2534017 |
| Goat polyclonal anti-rabbit IgG (H+L), HRP | Invitrogen | Cat#31460; RRID: AB_228341 |
| Goat polyclonal anti-mouse IgG (H+L), HRP | Invitrogen | Cat#A16072; RRID: AB_2534745 |
| Goat polyclonal anti-rabbit IgG (H+L), CF®568 | Biotium | Cat#20801; RRID: AB_3678764 |
| Donkey polyclonal anti-mouse IgG (H+L), CF®568 | Biotium | Cat#20802; RRID: AB_3678765 |
| **Bacterial and virus strains** | | |
| *Escherichia coli* BL21 (DE3) cells | Invitrogen | Cat#C600003 |
| pAAV-hSyn-mEGFP-WPRE | This paper | N/A |
| pAAV-hSyn-mEGFP-DLS-PBM-WPRE | This paper | N/A |
| pAAV-hSyn-mEGFP-DLS-PBM$^{d}$-WPRE | This paper | N/A |
| **Chemicals, peptides, and recombinant proteins** | | |
| Recombinant protein: PSD-95 (aa 1M-724L, UniProt: P78352) | Zeng et al.[7] | N/A |
| Recombinant protein: PSD-95_PSG (aa 309R-724L, UniProt: P78352) | Zeng et al.[7] | N/A |
| Recombinant protein: PSD-95_SH3-GK (aa 426N-724L, UniProt: P31016) | Zeng et al.[38] | N/A |
| Recombinant protein: PSD-95_GK (aa 531V-713G, UniProt: P31016) | Zhu et al.[37] | N/A |
| Recombinant protein: Stg_CT (aa 203D-323V, UniProt: Q3ZB20) | Zeng et al.[46] | N/A |
| Recombinant protein: np-GKAP (GKAP* AAS) | Wu et al.[61] | N/A |
| Recombinant protein: pi-GKAP (phosphorylated GKAP* AAS) | Wu et al.[61] | N/A |
| Recombinant protein: GKAP-95FR (replace GKAP* AAS 82R-89A with 95FR sequence) | This paper | N/A |
| Recombinant protein: Shank3-ME (6x PSD component, M1718E, with a N1315D to slightly enhance binding to Homer) | Zeng et al.[7] and this paper | N/A |

(*Continued on next page*)

*Continued*

| REAGENT or RESOURCE | SOURCE | IDENTIFIER |
|---|---|---|
| Recombinant protein: GB1-Shank3 (6x PSD component, with a N1315D to slighly enhance binding to Homer) | Zeng et al.[7] and this paper | N/A |
| Recombinant protein: Homer2 (aa 1M-354N, Uniprot: Q9QWW1) | This paper | N/A |
| Recombinant protein: Homer1a (aa 1M-186K, UniProt: Q9Z214) | Zeng et al.[7] | N/A |
| Recombinant protein: rCaMKIIα kinase domain (aa 1M-314S; UniProt: P11275) | Cai et al.[73] | N/A |
| Recombinant protein: Calmodulin (aa 1M-149K; UniProt: P0DP25) | Cai et al.[73] | N/A |
| Recombinant protein: PSD-95.FingR (95FR) | Zhu et al.[30] | N/A |
| Recombinant protein: PSD-93_GK (aa 659I-852L, UniProt: Q63622) | This paper | N/A |
| Recombinant protein: PSD-93_PSG (aa 418E-852L, UniProt: P78352) | Zeng et al.[38] | N/A |
| Recombinant protein: SAP97_GK (aa 700V-893L, UniProt: Q62696) | This paper | N/A |
| Recombinant protein: SAP102_GK (aa 656I-849L, UniProt: Q62936) | This paper | N/A |
| Recombinant protein: SAP102_PSG (aa 400R-849L, UniProt: Q62936) | Zeng et al.[38] | N/A |
| Recombinant protein: MAGI2-1-578 (aa 1M-578D, Uniprot: Q9WVQ1) | This paper | N/A |
| Recombinant protein: MAGI-2_PDZ0-GK (aa 1M-228I, UniProt: Q9WVQ1) | Zhang et al.[74] | N/A |
| Recombinant protein: MPP2_GK (aa 350R-542E, UniProt: Q9WV34) | This paper | N/A |
| Recombinant protein: MPP5_GK (aa 479K-660N, UniProt: Q8N3R9) | This paper | N/A |
| Recombinant protein: CASK_GK (aa 722R-900V, UniProt: Q62915) | This paper | N/A |
| Recombinant protein: MBP-DLS-PBM | This paper | N/A |
| Synthesized DLS-GS-PBM peptide (RIRREEYRRAINGQSFDLSGSKNYKQTSV) | Synthesized by QYAOBIO | N/A |
| Synthesized DLS-GSG-PBM peptide (RIRREAYRRAINGQSFDLSGSGKNYKQTS) | Synthesized by QYAOBIO | N/A |
| Synthesized DLS-GSGS-PBM peptide (RIRREAYRRAINGQSFDLSGSGSKNYKQTS) | Synthesized by QYAOBIO | N/A |
| Synthesized Myr-DLS-PBM peptide (Myr-GGGRIRREEYRRAINGQSFD LSGSKNYKQTSV) | Synthesized by QYAOBIO | N/A |
| Synthesized Myr-DLS-PBM$^{d}$ peptide (Myr-GGGRIRREAYRRAINGQSFDLSGSKNYKQTS) | Synthesized by QYAOBIO | N/A |
| iFlour™ 488 succinimidyl ester | AAT Bioquest | Cat#1023 |
| Cy3 succinimidyl ester | AAT Bioquest | Cat#271 |
| Alexa Flour™ 555 succinimidyl ester | AAT Bioquest | Cat#1023 |
| iFlour™ 488 succinimidyl ester | AAT Bioquest | Cat#1023 |
| Alexa Flour™ 647 succinimidyl ester | Invitrogen | Cat#A37566 |
| iFluor™ 488 maleimide | AAT Bioquest | Cat#1062 |
| iFluor™ 555 maleimide | AAT Bioquest | Cat#1063 |
| 5-Fluro-2′-deoxyuridine | Sigma-Aldrich | Cat#F0503 |
| Leibovitz L-15 medium | Gibco | Cat#21083027 |

(*Continued on next page*)

*Continued*

| REAGENT or RESOURCE | SOURCE | IDENTIFIER |
|---|---|---|
| Glutathione | Sigma-Aldrich | Cat#G4251 |
| Dulbecco's Modified Eagle Medium (DMEM) | ThermoFisher | Cat#12900017 |
| Neurobasal medium | Gibco | Cat#21103-0249 |
| B27 | Gibco | Cat#17504044 |
| GlutaMAX™ Supplement | Gibco | Cat#35050061 |
| Penicillin-Streptomycin | Gibco | Cat#15140122 |
| DNaseI | Sigma-Aldrich | Cat#DN25 |
| Trypsin | ThermoFisher | Cat#15090046 |
| Poly D-Lysine (PDL) | Sigma-Aldrich | Cat#P7280 |
| Hyclone™ Defined Fetal Bovine Serum (FBS) | Cytiva | Cat#SH30070.03 |
| Glucose Oxidase from Aspergilus niger | Sigma-Aldrich | Cat#G2133 |
| D-(+)-Glucose | Sigma-Aldrich | Cat#G8270 |
| Catalase from bovine liver | Sigma-Aldrich | Cat#C9322 |
| **Critical commercial assays** | | |
| Lipofectamine2000 transfection kit | Invitrogen | Cat#11668019 |
| ViaFect | Promega | Cat#E4982 |
| Helios Gene Gun Kit | Bio-Rad | Cat#1652411 |
| Helios Cartridge Kit | Bio-Rad | Cat#1652440 |
| **Deposited data** | | |
| PSD-95_GK/95FR complex structure | This paper | PDB: 9IUI |
| Raw Imaging Data | This paper | https://doi.org/10.17632/57p26ycbj9.2 |
| **Experimental models: Cell lines** | | |
| Human: HeLa cells | ATCC | CCL-2 |
| Human: HEK293T cells | ATCC | CRL-3216 |
| **Experimental models: Organisms/strains** | | |
| Mouse: C57BL/6J mice | Wuhan Youdu Biotechnoloty Co., Ltd | N/A |
| Rats: SD (Sprague Dawley) Rats | CUHK (The Chinese University of Hong Kong) | N/A |
| **Recombinant DNA** | | |
| Plasmid: 32M3C-PSD-95_FL | Zeng et al.[7] | N/A |
| Plasmid: M3C-PSD-95_PSG | Zeng et al.[7] | N/A |
| Plasmid: M3C-PSD-95_SH3-GK | Zeng et al.[38] | N/A |
| Plasmid: M3C-PSD-95_GK | Zhu et al.[37] | N/A |
| Plasmid: 32M3C-Stg_CT | Zeng et al.[46] | N/A |
| Plasmid: MG3C-GKAP_AAS | Wu et al.[61] | N/A |
| Plasmid: MG3C-GKAP-95FR | This paper | N/A |
| Plasmid: M3C-Shank3-ME (NPDZ-HBS-CBS-SAM, M1718E, N1315D) | Zeng et al.[7] and this paper | N/A |
| Plasmid: M3C-GB1-Shank3-WT (GB1-NPDZ-HBS-CBS-SAM, N1315D) | Zeng et al.[7] and this paper | N/A |
| Plasmid: M3C-Homer2 | This paper | N/A |
| Plasmid: M3C-Homer1a | Zeng et al.[7] | N/A |
| Plasmid: M3C-CaMKIIα | Cai et al.[73] | N/A |
| Plasmid: 32M3C-Camodulin | Cai et al.[73] | N/A |
| Plasmid: 32M3C-PSD-95.FingR_WT | Zhu et al.[30] | N/A |
| Plasmid: MBP3C-PSD-95.FingR_FE | This paper | N/A |
| Plasmid: 32M3C-PSD-93_PSG | Zeng et al.[38] | N/A |

(*Continued on next page*)

*Continued*

| REAGENT or RESOURCE | SOURCE | IDENTIFIER |
|---|---|---|
| Plasmid: M3C-PSD-93_GK | This paper | N/A |
| Plasmid: M3C-SAP97_GK | This paper | N/A |
| Plasmid: 32M3C-SAP102_PSG | Zeng et al.[38] | N/A |
| Plasmid: 32M3C-SAP102_GK | This paper | N/A |
| Plasmid: M3C-MAGI-2_PDZ0-GK | Zhang et al.[74] | N/A |
| Plasmid: M3C-CASK_GK | This paper | N/A |
| Plasmid: MBP3C-MPP2_GK | This paper | N/A |
| Plasmid: MBP3C-MPP5_GK | This paper | N/A |
| Plasmid: MBP3C-DLS-PBM | This paper | N/A |
| Plasmid: pCAG-GFP | This paper | N/A |
| Plasmid: pCAG-GFP-DLS-PBM | This paper | N/A |
| Plasmid: pCAG-GFP-DLS-PBM[d] | This paper | N/A |
| Plasmid: pCAG-mCherry | This paper | N/A |
| Plasmid: pCAG-mCherry-DLS-PBM | This paper | N/A |
| Plasmid: pCAG-mCherry-DLS-PBM[d] | This paper | N/A |
| Plasmid: pCMV-GFP-TM-Stg_CT | Chen et al.[5] | N/A |
| Plasmid: pCMV-PSD-95-GFP | This paper | N/A |
| Plasmid: pCMV-GFP-SAPAP1 | Wu et al.[61] | N/A |
| Plasmid: pCMV-GFP-Shank3 | This paper | N/A |
| Plasmid: pCMV-GFP-Homer1c | This paper | N/A |
| Plasmid: pCMV-mCherry | Wu et al.[61] | N/A |
| Plasmid: pCAG-95FR_WT-GFP | This paper | N/A |
| Plasmid: pCAG-95FR_FE-GFP | This paper | N/A |
| Plasmid: pCAG-95FR-GFP-CCR5TC | Gross et al.[60] | Addgene: #46295 |
| Plasmid: pCAG-iRFP670-SAPAP3-WT | This paper | N/A |
| Plasmid: pCAG-iRFP670-SAPAP3-SA | This paper | N/A |
| Plasmid: pCAG-iRFP670-SAPAP3-95FR | This paper | N/A |
| Plasmid: pCAG-iRFP670-SAPAP3-95FR-FE | This paper | N/A |
| Plasmid: pCAG-HA-SAPAP3-WT | This paper | N/A |
| Plasmid: pCAG-HA-SAPAP3-SA | This paper | N/A |
| Plasmid: pCAG-HA-SAPAP3-95FR | This paper | N/A |
| Plasmid: pCAG-HA-SAPAP3-95FR-FE | This paper | N/A |
| Plasmid: pCAG-PSD-95-mCherry | This paper | N/A |
| Plasmid: pCAG-iRFP670 | Chen et al. | N/A |
| Plasmid: pCAG-GFP-SAPAP3-WT | This paper | N/A |
| Plasmid: pCAG-GFP-SAPAP3-95FR | This paper | N/A |
| **Software and algorithms** | | |
| Origin7.0 | OriginLab | http://www.originlab.com/ |
| PyMOL | PyMOL | http://www.pymol.org/ |
| ImageJ | NIH | https://imagej.nih.gov/ij/ |
| GraphPad Prism | GraphPad Software Inc | http://www.graphpad.com/scientific-software/prism/ |
| ASTRA6 | Wyatt | http://www.wyatt.com/products/software/astra.html |
| Matlab | MathWorks | https://ww2.mathworks.cn/products/matlab.html |
| Phaser | McCoy et al.[75] | https://smb.slac.stanford.edu/facilities/software/ccp4/html/phaserwiki/index.html |
| Coot | Emsley et al.[76] | https://www2.mrc-lmb.cam.ac.uk/personal/pemsley/coot/ |
| Refmac5 | Murshudov et al.[77] | https://www2.mrc-lmb.cam.ac.uk/groups/murshudov/content/refmac/refmac.html |

(*Continued on next page*)

*Continued*

| REAGENT or RESOURCE | SOURCE | IDENTIFIER |
|---|---|---|
| Phenix.refine | Afonine et al.[78] | https://phenix-online.org/documentation/reference/refinement.html |
| MolProbity | Williams et al.[79] | http://molprobity.biochem.duke.edu/ |

## EXPERIMENTAL MODEL AND STUDY PARTICIPANT DETAILS

### Bacterial Strain

*Escherichia coli* BL21-CodonPlus (DE3)-RL cells (Agilent Technologies) were used in this study for the production of recombinant proteins. Cells were cultured in LB medium supplemented with necessary antibiotics.

### Cell line

Human HeLa cells were used in this study for confocal based imaging assays. Cells were cultured in DMEM medium supplemented with 10% fetal bovine serum at 37 °C with 5% $CO_2$. Human HEK293T cells were used in this study for AAV generation.

## METHOD DETAILS

### DNA constructs and chemical agents

DNA fragments encoding recombinant proteins were generated via the standard PCR-based methods and inserted into pET-based vectors containing N-terminal $His_6$-, TRX-$His_6$-, MBP-$His_6$- or GB1-$His_6$-tag each followed by an HRV-3C protease cleavage site. The PSD-95.FingR gene was amplified from pCAG-PSD-95.FingR-eGFP-CCR5TC (Addgene #46295) by standard PCR. For expression in cultured neurons and hippocampal slices, DLS-PBM and DLS-PBM$^d$ sequences were synthesized and inserted downstream of the CAG promoter. PSD-95.FingR with its C-terminus tagged with EGFP was inserted after the CAG promoter. PSD protein sequences were inserted downstream of CMV promoter. For HeLa cells expression, PSD-95 with its C-terminus tagged with mCherry, and SAPAP3 variants with its N-terminus tagged with GFP or iRFP670 were inserted after the CAG promoter. For AAV preparation, mEGFP, mEGFP-DLS-PBM, and mEGFP-DLS-PBM$^d$ were constructed and inserted to pAAV-hSyn-3xFLAG-WPRE (Addgene # 127862) backbone (between EcoRI/HindIII sites). All constructs were verified by DNA sequencing.

The DLS-PBM-related peptides (for biochemical assays), Myr-DLS-PBM and Myr-DLS-PBM$^d$ peptides (for electrophysiology) were synthesized by QYAOBIO with purity >95%.

### Protein expression and purification

Recombinant proteins were expressed in Escherichia coli BL21-CodonPlus (DE3)-RIL (Agilent) in auto induction media LB (Cat#AIMLB0210, FORMEDIUM) at 16 °C overnight after cells were cultured at 37 °C to $OD_{600}$ between 0.6-0.8. Generally, each recombinant protein was purified using a nickel-NTA agarose affinity column followed by a size-exclusion chromatography (Superdex 200 or Superdex 75) with a column buffer containing 50 mM Tris, pH 7.8, 100 mM NaCl, 1 mM EDTA, 1 mM DTT.

For purification of PSD-95 (Uniprot: P78352-1), after size-exclusion chromatography by Superdex 200 following cleavage by HRV 3C protease at 4 °C overnight, a mono Q ion-exchange chromatography was applied to remove Trx-$His_6$ affinity tag, DNA contamination and degraded proteins. Proteins were exchanged into a buffer containing 50 mM Tris, pH 7.8, 100 mM NaCl, 1 mM EDTA, 1 mM DTT by a HiTrap desalting column.

For purification of Stg (NCBI: NP_031609, 203D-323V),cells were grown in LB medium at 37 °C until $OD_{600}$ around 0.8 before induction of protein expression by 0.5 mM IPTG at 37 °C for 3 hours. Proteins eluted from the affinity column were then purified by Superdex 75 size-exclusion chromatography with a column buffer containing 50 mM Tris, pH 7.8, 300 mM NaCl, 1 mM EDTA, 1 mM DTT. After affinity tag cleavage by HRV 3C protease, a mono S ion-exchange chromatography was used to remove the Trx-$His_6$ tag. Proteins were exchanged into a working buffer containing 50 mM Tris, pH 7.8, 100 mM NaCl, 1 mM EDTA, 1 mM DTT by a HiTrap desalting column.

Recombinant PSD-95.FingR was purified using $Ni^{2+}$-NTA affinity column followed by size-exclusion column (Superdex 75) in buffer containing 50 mM Tris, pH 7.8, 100 mM NaCl, 1 mM EDTA, 2 mM DTT. After the cleavage of the affinity tag by HRV 3C protease, a ResourceS column was used to separate the remaining contaminating proteins and the cleaved affinity tag. To purify F72E mutant of PSD-95.FingR, a size-exclusion column (Superdex 75) was used to separate the affinity tag after the cleavage by HRV 3C protease.

To co-purify the complex of PSD-95.FingR/PSD-95_GK, the suspended cultured bacterial were mixed and homogenized in lysis buffer. The mixed lysate was further purified by using $Ni^{2+}$-NTA affinity chromatography followed by a step of size-exclusion chromatography (Superdex 75) with column buffer containing 50 mM Tris, pH 7.8, 100 mM NaCl, 1 mM EDTA, 2 mM DTT. The affinity tag was cut by HRV 3C protease and removed by an additional size-exclusion column (Superdex 75) in buffer containing 50 mM Tris, pH 7.8, 100 mM NaCl, 1 mM EDTA, 2 mM DTT.

### Isothermal titration calorimetry assay

ITC measurements were carried out on a MicroCal VP-ITC calorimeter at 25 °C. Proteins used for ITC measurements were dissolved in an assay buffer composed of 50 mM Tris, pH 7.8, 100 mM NaCl, 1 mM EDTA, and 1 mM DTT. Affinity tags on proteins were cleaved and removed. High concentration of protein was loaded into the syringe and titrated into the cell containing low concentration of corresponding interactors (concentrations for each reaction are indicated in the figure legends). For each titration point, a 10 μL aliquot of a protein sample in the syringe was injected into the interacting protein in the cell at a time interval of 2 min. Titration data were analyzed using the Origin7.0 software and fitted with the one-site binding model.

### Size exclusion chromatography coupled with multi-angle light scattering (SEC-MALS) assay

The SEC-MALS system is composed of a static light scattering detector (MiniDawn, Wyatt), a differential refractive index detector (Optilab, Wyatt), and an AKTA purifier (GE Healthcare). 100 μL sample was injected into a Superose 12 Increase 10/300 GL or Superose 6 increase 10/300 GL column pre-equilibrated with a column buffer containing 50 mM Tris, pH 7.8, 100 mM NaCl, 1 mM EDTA, 1 mM DTT. Data were analyzed by the ASTRA6 (Wyatt) software.

### Protein crystallization and structure determination

The crystals of the PSD-95_GK/95FR complex were obtained by hanging drop vapour-diffusion method at 16 °C. PSD-95_GK/95FR protein complex solution with the concentration of 20 mg/mL was mixed with the reservoir buffer containing 0.1 M Sodium citrate tribasic dihydrate (pH 5.2) and 18% PEG 8000 with the ratio of 1μL and 1μL for crystallization.

Crystals were cryoprotected with 25 % glycerol and flash-cooled to 100 K. X-ray diffraction data were collected at BL19U1 beamlines at Shanghai Synchrotron Radiation Facility (SSRF). Diffraction data were processed using XDS program package (Kabsch, 2010). Structures were solved by molecular replacement method using Phaser.[75] The crystal structure of PSD-95 GK (PDB ID: 5YPO) and a structure of FNIII domain (PDB ID: 4MMX) were used as the searching model. Manual model building and refinement were carried out iteratively using Coot,[76] Refmac5[77] and Phenix.refine.[78] The final models were validated by MolProbity,[80] and statistics were summarized in Table S1. The figures were produced using PyMOL (http://www.pymol.org/).

### AAV preparation

rAAVs were generated according to established protocol.[81] In brief, HEK293T cells were triple transfected using polyethylenimine; virus was collected after 120 h from both cell lysates and media and purified over iodixanol (OptiPrep, Sigma-Aldrich).

### Slice culture and transfection

Hippocampal organotypic slice cultures were prepared from 7-9 day old rats as previously described.[82] Transfections were carried out 48 h after slicing. Briefly, 50 μg DNA was coated on 1 μm diameter gold particles in 0.5 mM spermidine, precipitated with 0.1mM $CaCl_2$, and washed four times in pure ethanol. The gold particles were coated onto PVC tubing, dried using ultra-pure $N_2$ gas, and stored at 4°C in desiccant. DNA-coated gold particles were delivered with a Helios Gene Gun (BioRad). Slices were maintained at 34 °C with media changes every two days.

### Acute slice preparation

Acute hippocampal slices were prepared from P18-P28 mice. Mice were anesthetized with isoflurane. Brains were collected and sliced into 300 μm near-horizontal sections using Microslicer DTK-Zero1 (Ted Pella). Slices were then transferred to a holding chamber containing ACSF (in mM) (125 NaCl, 2.5 KCl, 1.25 $NaH_2PO_4$, 25 $NaHCO_3$, 11 glucose, 1 $MgSO_4$, 2 $CaCl_2$ saturated with 95% $O_2$/5% $CO_2$) and incubated for 20 minutes at 37°C and then kept at room temperature until use.

### Electrophysiological recording

All electrophysiological recordings were carried out on an upright Olympus BX51WI microscope and collected using a Multiclamp 700B amplifier (Molecular Devices). During recording, slices were maintained in ACSF (in mM): 125 NaCl, 2.5 KCl, 1.25 $NaH_2PO_4$, 25 $NaHCO_3$, 11 glucose saturated with 95% $O_2$; 5% $CO_2$ containing 1 $MgSO_4$, 2 $CaCl_2$ during acute slice recordings and 4 $MgSO_4$, 4 $CaCl_2$ during slice culture recordings. Transfected cells were identified visually using fluorescence and recorded simultaneously with a neighboring control cell. All recordings were carried out at 20-25 °C using glass patch electrodes filled with an intracellular solution (in mM): 135 $CsMeSO_3$, 10 HEPES, 8 NaCl, 0.3 EGTA, 4 Mg-ATP, 0.3 Na-GTP, 5 QX-314, and 0.1 spermine. Synaptic currents were elicited by stimulation of the Schaffer collaterals with a bipolar electrode (Micro Probes). AMPAR- and NMDAR-mediated responses were collected in the presence of 100 μM picrotoxin to block inhibition. 5 μM 2-chloroadenosine was used to suppress epileptic activity in slice culture. The bipolar stimulating electrode was placed in stratum radiatum. AMPAR EPSCs were evoked while voltage clamping cells at -70 mV, and the amplitude was determined by measuring the peak of the response. NMDAR EPSCs were obtained while voltage clamping cells at +40 mV and measured at 100 ms. Series resistances typically ranged from 10 to 20 MΩ; a cell pair was discarded if the series resistance of either cell increased to >30 MΩ. Statistical difference was determined using a two-tailed paired t test.

LTP was induced via a pairing protocol of 2 Hz stimulation for 90 s at a holding potential of 0 mV, after recording a 3-5 min baseline, but not more than 6 min after breaking into the cell. All LTP experiments were carried out in acute slices. Simultaneous dual whole-cell

recordings were made in a transfected CA1 pyramidal cell and a neighboring wild-type cell. In some cases, one of the paired cells was lost during the experiment, then the recordings were considered until that point. In cases where one cell was lost the remaining cell was considered for the averages.

## Behavioral analyses

### *Stereotaxic injection*

Stereotaxic injections were performed to deliver adeno-associated viruses (AAV) expressing GFP, GFP-DLS-PBM, or GFP-DLS-PBM$^{d}$ into the CA1 region of the hippocampus in 3-month-old male mice. The viral titers were standardized and diluted to a final concentration of $2 \times 10^{12}$ vg/ml for all constructs. Mice were anesthetized with isoflurane (induction at 3%, maintenance at 1-2% in oxygen) and placed in a stereotaxic apparatus (RWD, China). The skull was exposed, and small burr holes were drilled at the following coordinates relative to bregma: anteroposterior (AP) -2.0 mm, mediolateral (ML) ±1.5 mm, and dorsoventral (DV) -1.5 mm from the skull surface. A total volume of 0.5 μl of virus was injected bilaterally into the CA1 region at a rate of 0.1 μl/min using a 10 μl microsyringe (Hamilton, USA) and an automatic syringe pump (Harvard Apparatus, USA). After injection, the needle was left in place for an additional 5 minutes to allow for virus diffusion before being slowly withdrawn. The scalp was then sutured, and mice were allowed to recover on a warm pad before being returned to their home cages.

Following stereotaxic injection, mice were housed individually and monitored daily to ensure proper recovery. Viral expression was allowed to proceed for three weeks. After this incubation period, mice were subjected to behavioral testing to assess the effects of the viral constructs. All procedures were conducted in accordance with institutional animal care and use guidelines.

### *Novel object recognition test*

The novel object recognition test was conducted to assess recognition memory in male mice aged 120 ± 5 days. Mice were first acclimated to the testing environment by being placed in an open-field arena (50 × 50 × 38 cm) facing the wall and allowed to explore freely for a 5-minute habituation period. During the training session, mice were exposed to two identical objects placed near the corners of the arena, each positioned 3 cm from the adjacent walls. Mice were allowed to explore the arena and the objects for 5 minutes. Following a delay period of 1 hour, the mice underwent a 5-minute test session in which two objects were placed in the same positions as in the training session, but one of the objects was replaced by a novel object. The type and position of the novel object were counterbalanced across all experiments to avoid spatial and object biases.

Explorative behavior was defined as the mouse approaching the object with its nose pointed at a maximum distance of 2.5 cm from the object. The time spent exploring each object was recorded using an automated video tracking system positioned above the arena. The recognition discrimination index (DI) was calculated as (T2 - T1) / (T1 + T2), where T1 is the time spent exploring the familiar object, and T2 is the time spent exploring the novel object. A positive discrimination index indicates a preference for the novel object, reflecting recognition memory. All sessions were conducted under consistent lighting and noise conditions to minimize external influences on the mice's behavior.

### *Y-maze test*

The Y-maze test was conducted in a symmetrical Y-shaped apparatus consisting of three identical arms (33.5 cm in length, 5 cm in width, 15 cm in height), arranged at 120-degree angles relative to each other. Each arm was equipped with movable gates, and distinct geometric patterns were used as visual cues on the inner walls of the arms.

The novel arm spatial recognition test comprised an exploration phase and a test phase. During the exploration phase, one arm was closed and designated as the novel arm, while the two open arms were labeled as the start arm and the other arm. Mice were placed at the end of the start arm facing the wall and allowed to freely explore the two open arms for 5 minutes. After a 1-hour interval, the test phase was initiated by opening the novel arm. Mice were reintroduced into the maze from the same starting position and allowed to explore all three open arms for 5 minutes. Each mouse was removed after the test, and the apparatus was wiped with 75% ethanol to prevent olfactory cues. The entire experiment was recorded using an overhead camera, which tracked the movement and activity of the mice. The number of entries and the duration of stay in each arm were analyzed, and a recognition index was calculated as (Time in Novel Arm - Time in Other Arm) / (Time in Novel Arm + Time in Other Arm).

## Primary hippocampal neuron culture

Primary hippocampal neuron cultures were prepared from embryonic day 19 (E19) Sprague Dawley rats hippocampi. Dissociated cells were plated on poly-D-lysine (PDL) coated coverslips (for fixed sample) or glass bottom petri dish (for live cell imaging, TKO-P351173-413, MatTek) in neurobasal media (Gibco) supplemented with 1% penicillin-streptomycin (10,000 U/ml) (Gibco), 1% GlutaMax Supplement (Gibco), 2% B27 Supplement (Gibco) and 10% fetal bovine serum (FBS, Hyclone). Four hours after plating, the medium was replaced with medium lacking FBS. Neurons were maintained in an incubator at 37 °C with 5% $CO_2$, and medium was changed every three days over the duration of the culture. Especially, at DIV7, 2.5 μM 5-Fluoro-2'-deoxyuridine (FdU, final concentration) was applied into culture media to inhibit proliferation of glial cells. Generally, cells were transfected at DIV14-18 with Lipofectamine 2000 (Invitrogen) in accordance with manufacture's manual. After 3-4 days, cells were subject to live cell imaging or fixed with 4% (vol/vol) paraformaldehyde (PFA) together with 4% (wt/vol) sucrose in 1x PBS (pH 7.5) and then mounted on slides for confocal imaging.

### HeLa cell culture

HeLa cells were cultured in DMEM medium supplemented with 10% fetal bovine serum at 37°C with 5% $CO_2$. Each well of cells was co-transfected with 0.5 μg PSD-95-mCherry plasmid, 0.5 μg iRFP670-SAPAP3 plasmid, and 0.5 ug GFP-Shank3 plasmid at 60% cell confluency using ViaFect transfection kit following the instruction of the manual. Transfected cells were fixed with 4% paraformaldehyde, 4% sucrose in PBS at 20 h after transfection. A Zeiss LSM 880 confocal microscope with a 63x oil lens was used for imaging of fixed cells. For live cell imaging, HeLa cells were incubated in a humidified chamber with 5% $CO_2$ at 37 °C at 12-14 h after transfection. Time-lapse imaging was performed by Zeiss LSM 880 microscope with a 40x oil lens.

### Immunocytochemistry

#### *Live cell staining*

For AMPA receptor single-molecule tracking assay, anti-GluA1-NT antibody (MAB2263, Sigma-Aldrich, 1:500 dilution) was applied in culture media supplemented with 1% (vol/vol) FBS at 37 °C for 15 minutes, followed by twice of washing with culture media. CF568-conjugated secondary antibody (Cat#20802, Biotium, 1:500 dilution) was then applied in culture media supplemented with 1% (vol/vol) FBS at 37 °C for 15 minutes. After twice of washing with culture media, the cells were subject for single molecule localization microscopy (SMLM) live imaging.

#### *Fixed sample staining*

For surface GluA1 staining, anti-GluA1-NT antibody (MAB2263, Millipore, 1:500 dilution) was applied in culture media supplemented with 1% (vol/vol) FBS at 37 °C for 15 minutes followed by fixation. For endogenous PSD-95, pan-Shank, total GluA1, RIM1 and overexpressed HA-tagged SAPAP3 staining, after fixation, cells were blocked and permeabilized in PBS containing 10% (wt/vol) normal donkey serum (NDS) and 0.2% (vol/vol) Triton X-100 at room temperature for 1h, followed by incubation with primary antibody (anti-PSD-95, MAB1596, Millipore, 1:2000 dilution for confocal microscopy or 1: 500 for dSTORM microscopy; anti-pan-Shank, cat# 851902, BioLegend, 1:1000 dilution; anti-GluA1-NT antibody, MAB2263, Millipore, 1:500 dilution; anti-panSynGAP, PA1-046, Invitrogen, 1:1000 dilution; anti-RIM1, 140003, SYSY, 1:500 dilution; anti-HA, H6908, Sigma-Aldrich, 1:1000) in PBS containing 3% NDS and 0.2% Triton x-100 at 4 °C overnight. After three times washing with PBS, cells were incubated with fluorescence-conjugated secondary antibodies (anti-rabbit Alexa488, A21206, Thermo Fisher, 1:500 dilution; anti-mouse Alexa568, A10037, Thermo Fisher, 1:500 dilution; anti-rabbit Alexa568, A10042, Thermo Fisher, 1:500 dilution; anti-mouse Alexa647, A31571, Thermo Fisher, 1:500 dilution; anti-rabbit CF568, #20801, Biotium, 1:500 dilution for RIM1 staining and 1:1000 dilution for HA-tagged SAPAP3 dSTORM staining) in PBS containing 3% NDS and 0.2% Triton x-100 at room temperature for 1h, followed by three times washing with PBS and then either mounted on slides for confocal imaging or directly subjected for dSTORM imaging.

### PSD preparation

PSD extraction procedures follow the protocol from.[83] Cells were collected from collected and homogenized by passage through a 26 g needle 12 times in homogenization buffer (320 mM sucrose, 1 mM EDTA, 10 mM HEPES, pH 7.4, 200 nM okadaic acid, protease inhibitor cocktail). The homogenate was centrifuged at 800 xg for 10 minutes at 4 °C. The supernatant was further centrifuged at 15,000 xg for 20 minutes at 4 °C. The pellet was resuspended in 4 mM HEPES, pH 7.4, and incubated with agitation at 4 °C for 30 minutes, followed by centrifugation at 25,000 xg for 20 minutes at 4 °C. The pellet was resuspended in 50 mM HEPES, pH 7.4, mixed with an equal volume of 1% (vol/vol) Triton X-100, and incubated with agitation at 4 °C for 15 minutes. The PSD fraction was generated by centrifugation at 32,000 xg for 20 minutes at 4 °C. The final PSD pellet was resuspended in 50 mM HEPES, pH 7.4, followed by analysis with Western blot. Antibodies: pan-SynGAP (Cat# PA1-046, Invitrogen, 1:1000 dilution), PSD-95 (MAB1596, Millipore, 1:1000 dilution), beta-actin (60008-1-Ig, Proteintech, 1:2000 dilution), goat anti-mouse IgG (H+L) secondary antibody HRP (Cat#31460, Invitrogen, 1:20,000 dilution), goat anti-mouse IgG (H+L) secondary antibody HRP (Cat#A16072, Invitrogen, 1:20,000 dilution).

### Fluorescence recovery after photobleaching (FRAP) assay

FRAP assay was performed on a Zeiss LSM 880 confocal microscope. Live cells grown on glass bottom culture dish (MatTek) were maintained at 37 °C with 5% $CO_2$ for imaging. PSD-95-GFP and GFP-Shank3 in dendritic spine were selected as region of interest (ROI) for bleaching and recording. To measure the dynamics of PSD-95 in Shank3 puncta in HeLa cells, the PSD-95-mCherry in Shank3 puncta were selected as ROI for bleaching and recording. The fluorescent intensity difference between pre-bleaching and at time 0 (the time point right after photobleaching pulse) was normalized to 100%.

### Protein fluorescence labeling

#### *Amide labeling*

Highly purified proteins were exchanged into a HEPES buffer (containing 20 mM HEPES, pH 7.5, 300 mM NaCl, 1 mM EDTA and 1 mM DTT) and concentrated to 5-10 mg/mL. iFluor-488 and Cy3 NHS Ester (AAT Bioquest) and Alexa Fluor 647 NHS Ester (ThermoFisher) were dissolved by DMSO to make stock solutions at the concentration of 10 mg/mL. Each dye and the protein to be labeled were mixed at a molar ratio of 1:1 and the reaction lasted for 2 hours at room temperature. Reaction was quenched by 200 mM Tris, pH 8.2. The fluorophores and other small molecules were removed from the proteins by passing the reaction mixture through a HiTrap desalting column with buffer containing 50 mM Tris, pH 7.8, 100 mM NaCl, 1 mM EDTA, 1 mM DTT.

### *Cysteine labeling*

$His_6$-Stg and $His_8$-PSD-95 were prepared in a labeling buffer (50 mM Tris pH 7.5, 300 mM NaCl, 1 mM TCEP). Alexa Fluor 488 maleimide or Alexa Fluor 555 maleimide (Invitrogen) (stock solution with 10 mg/mL in DMSO) was added with 1:1 protein-to-fluorophore molar ratio and incubated for 2 hours at room temperature. The fluorophores and other small molecules were removed from the proteins by passing the reaction mixture through a HiTrap desalting column with buffer containing 50 mM Tris, pH 7.8, 100 mM NaCl and 1 mM TCEP.

Fluorescence labeling efficiency was measured by Nanodrop One$^c$ Microvolume UV-Vis Spectrophotometer (ThermoFisher). In imaging assays, fluorescence labeled proteins were further diluted with the corresponding unlabeled proteins in the same buffer. Dilution ratio was specified in the legend of each figure.

## In vitro GKAP/SAPAP1 phosphorylation

In vitro GKAP phosphorylation assay was as previously described.[61] The kinase domain of CaMKIIα was mixed and activated by Calmodulin (with 1:2 molar ratio) in a buffer containing 50 mM Tris pH 7.8, 100 mM NaCl, 10 mM ATP, 5 mM $CaCl_2$, 5 mM $MgCl_2$, 1 mM DTT at room temperature for 10 minutes. GKAP protein (a recombinant version of GKAP compatible for *in vitro* phosphorylation[61]) at 40 μM was mixed with 1 μM auto-phosphorylated CaMKIIα kinase domain in a reaction buffer containing 50 mM Tris pH 7.5, 100 mM NaCl, 10 mM ATP, 5 mM $MgCl_2$ and 1 mM DTT at room temperature overnight. To remove the enzymes after phosphorylation, samples were passed through a Superdex 75 size-exclusion column with buffer containing 50 mM Tris, pH 7.8, 100 mM NaCl, 1 mM DTT and 1 mM EDTA.

## Imaging-based assay of phase separation

Imaging-based phase separation assays followed our previously described procedures.[7] Briefly, proteins (with affinity tags cleaved and removed) were prepared in a buffer containing 50 mM Tris, pH 7.8, 100 mM NaCl, 1 mM EDTA, 1 mM DTT and pre-cleared via high-speed centrifugation. Proteins were then mixed and diluted with buffer to designated combinations and concentrations. For imaging assay, protein samples were injected into a homemade flow chamber for fluorescent imaging with a Zeiss LSM880 confocal microscope (63x lenses) at room temperature. Images and fluorescence intensities of signals were analyzed by the ImageJ software.

## Single molecule tracking assay

### *GluA1 single molecule tracking in living neurons*

Living neuron samples were transferred to the Leibovitz L-15 medium (Cat #21083027, Gibco) supplemented with 10 mM glutathione (G4251, Sigma-Aldrich) and loaded onto a ZEISS Elyra7 microscope with a live cell supporting system. During the imaging process, the system temperature was maintained at 37 °C, the $CO_2$ level was maintained at 5%. A wide field image with low laser power was captured before tracking, which will be used as the reference to align the tracks with the region of interest. A bleaching process was performed with 50% of 561nm laser power to eliminate overlapped single molecule signals followed by 20% of 561nm laser power to stochastically emit CF568 single molecule fluorescence with long on time. Each single molecule tracking experiment was recorded with 2000 frames of images with an exposure time of 30 ms for each image. Definite-focus system was on during the imaging process. All data were collected within 1 hour imaging session for each sample.

### *PSD-95 and Stg_CT single molecule tracking in the reconstituted PSD condensate*

Reconstituted PSD condensates was transferred into a homemade chamber and loaded onto a ZEISS Elyra7 microscope. A wide field image with a low laser power was captured before tracking. A bleaching process was performed with 100% of 561nm laser power to eliminate overlapped single molecule signals followed by 50% of 561nm laser power to stochastically emit Alexa 555 or Cy3 single molecule fluorescence with long on time. Each single molecule tracking experiment was recorded with 3000 frames of images with an exposure time of 30 ms per image. Definite-focus system was on during the imaging process. All data were collected within 1 hour imaging session for each sample.

Raw data for the living neuron and the reconstituted PSD condensates tracking experiments were first processed with the software comes with the ZEISS Elyra7 microscope. The threshold of the signal to noise ratio was set as 5.0 and the overlapped signals were recognized as multiple localizations. Single molecule tracking analysis was performed with a customized programme as described previously (https://github.com/NeoLShen/Code-for-phase-simulation-and-HMM-analysis).[27]

## 3D dSTORM imaging

Fixed neuron samples were transferred into an imaging buffer with 5% D-glucose (Sigma, G8270), 0.56 mg/mL glucose oxidase (Sigma, G2133-50KU), 40 μg/mL catalase (Sigma C9322-10G), and 143 mM β-mercaptoethanol in PBS. Imaging of each sample was completed within an hour upon the addition of the imaging buffer.

For 2D dSTORM analysis of HA-SAPAP3 and PSD-95 localization in synapses, a Zeiss Elyra7 microscope with a 63x (N.A.=1.4) oil objective lens was used to capture and analyze the dual channel images. A wide-field image was captured first with 2% of the full power (500mW) of 488nm/561nm/647nm laser. dSTORM images were acquired under 100% of the full power of 561nm/647nm laser with the HILO mode and a TIRF-hp filter were used during imaging. All images were captured with 12,000 frames with an exposure

time of 30ms per frame. Auto focus with the ''definite focus'' strategy was performed at every 300 frames. Alignment of dual channels was performed before imaging. Maximum PSF size was set at 9 and SNR was set at 6 when capturing single molecules with Zeiss Elyra7.

For 3D dSTORM analysis of endogenous PSD-95 and RIM1 clusters in synapses, a Nikon N-STORM microscope with a 100x (N.A.=1.4) oil objective lens was used to capture and analyze the dual channel images. A wide field image with 3% of 488nm/561nm/647nm laser power was captured as a reference at the beginning. A bleaching process was performed with 100% of 647nm/561nm laser power to the sample for 1 minute. Each dSTORM image was recorded with 20,000 frames with an exposure time of 20 ms per frame under the 3D-dSTORM mode. Perfect-Focus-System was used to maintain the z dimension focus during imaging. All data were collected within a 2-hour imaging session for each sample. Raw images were processed with the Nikon's NIS-Elements AR 6.02.00 software. 3D calibration and channel alignment were performed before all images were acquired. Drift correction was performed using auto-correlation algorithms. Output localization list was then processed with a customized MATLAB program to select individual synapses (https://github.com/NeoLShen/3D-STORM-data-process-with-MATLAB-app.git).[61] Nanocluster analysis was performed with the same code and the same criteria as reported in the literature.[62]

### Quantification of dSTORM imaging for cultured neuron

Synapses were first manually tagged with the wide-field image. The cluster of super-resolution localizations in synapses were then selected manually with the help of tessellation-based auto clustering algorithm.[84,85] Mask of spine or shaft boundaries were generated by wide-field GFP signal with manually set thresholds.

An overlap coefficient was introduced to quantitatively compare the molecule distributions captured by dSTORM imaging. Two pixelated (pixel size of 20 nm x 20 nm) two-dimensional localization density maps were calculated with the selected localizations for each channel. The density maps were then normalized with their total number of localizations of each channel. The overlap coefficient was defined as the summary of the overlapping value of each pixel between two normalized density maps. This overlap coefficient will only be affected by the two normalized density distributions and will only have a single number to describe the degree of overlapping between two distributions.

Nanocluster was identified by a local density-based algorithm coded with MATLAB that is commonly used in synaptic cluster analysis.[62] After identifying synaptic region and nanocluster localizations of STORM signal, nanocluster number (NC number) was defined as the number of isolated nanocluster in each synaptic region. Nanocluster volume (NC volume) was defined as the summation of all nanocluster's volume (calculated by the alpha-shape volume of each nanocluster's localizations) in the same synaptic region. Synaptic volume was calculated by the alpha-shape volume of all localizations in each synaptic region. The ''NC volume / Synaptic volume'' was defined as the ratio of nanocluster volume over synaptic volume. For demonstration of the ''Top View'' of each paired pre- and postsynaptic nanocluster distribution, a heat map was used to represent the local density of each localization in paired synaptic regions.

## QUANTIFICATION AND STATISTICAL ANALYSIS

For quantification of spine enrichment in Figures 2A, 2B, 3A, 3B, 6G, and S6K–S6M the enrichment fold was defined as the ratio of average fluorescent intensity in dendritic spine divided by the average fluorescent intensity in dendritic shaft. The background intensity was subtracted. The enrichment fold of 20-30 spines from one neuron was averaged as one data point. We used the cytosolic tail of Stargazin fused with transmembrane domain of PDGFR to increase its synaptic localization.[5,86]

For quantification of positive spine ratio in Figures 3C, 3D, 5G–5I, S3C, and S3D, images were thresholded with the same setting, to make dendritic shaft signal around invisible. After that, 30-50 spines of one neuron are counted for positive spine ratio as one data point. For quantification of spine width in transfected neurons, a dendrite of 20-40 μm was picked for analysis. The average width of all selected spines was calculated as the spine width or enrichment fold in each neuron. For each neuron, 2-4 dendrites were analyzed. The numbers of neurons picked were specified in the figure legends.

For quantification of enrichment of overexpressed proteins in cellular Shank3 puncta in Hela cells, 7 regions with pixel size of 10 x 10 were selected for each cell. Within 7 regions, 5 regions were selected from Shank3 puncta, 1 region was selected from the cytosol, and 1 region was selected from the background out of cells. The mean fluorescence intensity (I) of proteins in each selected region was measured. The enrichment fold was calculated as $(I_{puncta}-I_{background})/(I_{cytosol}-I_{background})$.

Statistical parameters including the definitions and exact values of n (e.g., number of experiments, number of spines, number of cells, etc.), distributions and deviations are reported in the figures and corresponding figure legends. Data of in vitro phase separation imaging assay are expressed as mean ± SD. Data of primary mice neuron culture, mice behavior and electrophysiology are expressed as mean ± SEM. ns, not significant, *$p < 0.05$, **$p < 0.01$, ***$p < 0.001$ and ****$p < 0.0001$ using student T-test or one-way ANOVA with Tukey's multiple comparison test. Data are judged to be statistically significant when $p < 0.05$ by one-way ANOVA with Tukey's multiple comparison test. None of the data were removed from our statistical analysis as outliers. Statistical analysis was performed in GraphPad Prism. Experiments of neuronal culture imaging were performed in blinded fashion, except for the live cell-based and dSTORM assays.

**Molecular Cell, Volume *85***

## Supplemental information

# Modulating synaptic glutamate receptors by targeting network nodes of the postsynaptic density condensate

**Bowen Jia, Shihan Zhu, Zeyu Shen, Xiumin Chen, Hao Li, Shuaizhu Zhao, Qixu Cai, Yu Wang, Ziqi Wang, Roger A. Nicoll, Youming Lu, and Mingjie Zhang**

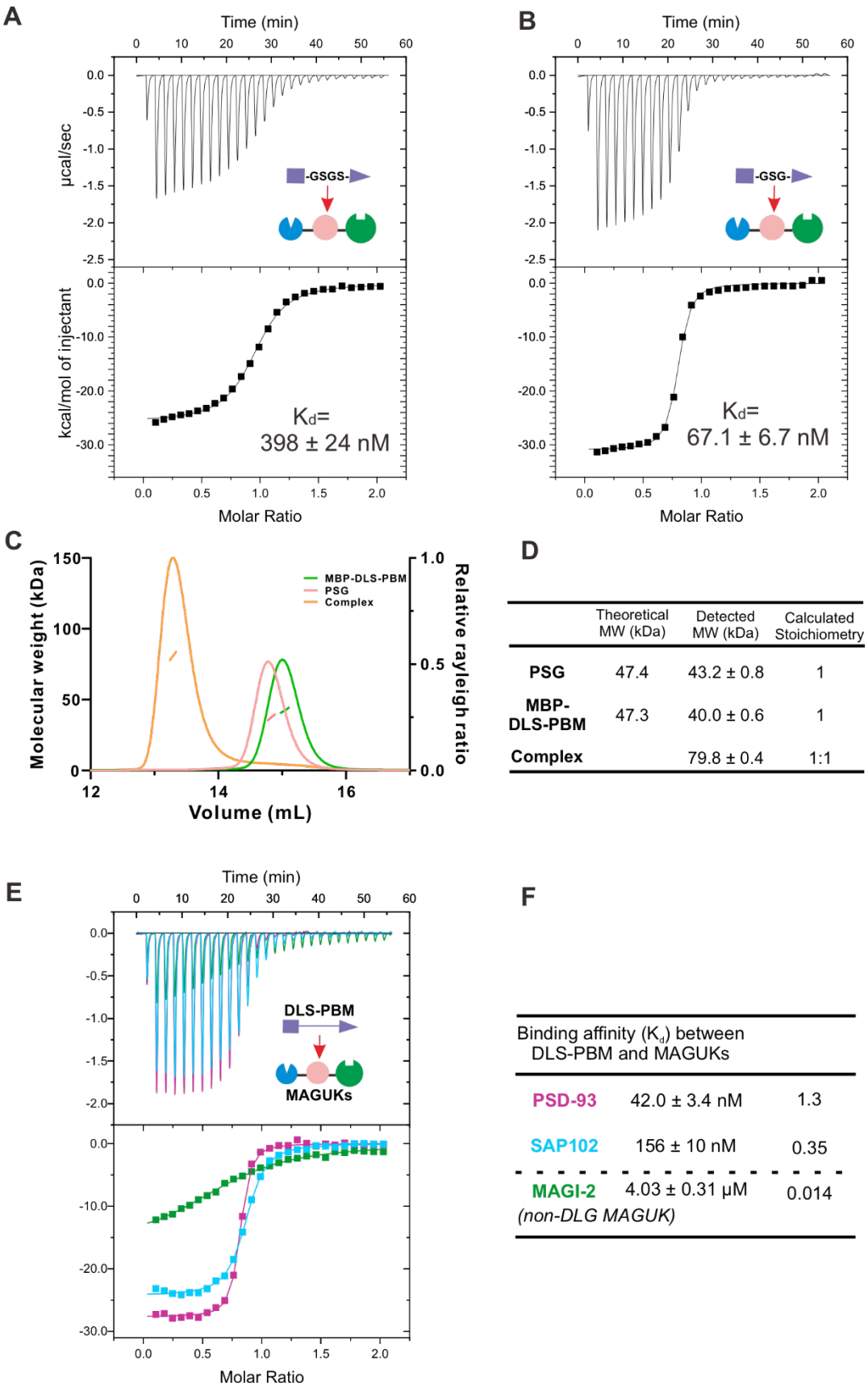


| | Theoretical MW (kDa) | Detected MW (kDa) | Calculated Stoichiometry |
|---|---|---|---|
| **PSG** | 47.4 | 43.2 ± 0.8 | 1 |
| **MBP-DLS-PBM** | 47.3 | 40.0 ± 0.6 | 1 |
| **Complex** | | 79.8 ± 0.4 | 1:1 |

| Binding affinity ($K_d$) between DLS-PBM and MAGUKs | | |
|---|---|---|
| PSD-93 | 42.0 ± 3.4 nM | 1.3 |
| SAP102 | 156 ± 10 nM | 0.35 |
| MAGI-2 *(non-DLG MAGUK)* | 4.03 ± 0.31 µM | 0.014 |

**Figure S1. Design and validation of DLS-PBM, related to Figure 1.**

**(A and B)** ITC-based measurement of the affinities of DLS-PBM with different length of linkers to the PSD-95 PSG supramodule.

**(C and D)** FPLC-coupled static light-scattering analysis showing that mixing equal molar of PSD-95 PS with MBP-tagged DLS-PBM leads to formation of a 1:1 PSG/DLS-PBM complex (orange curve). The elution profiles of isolated PSD-95 PSG (pink curve) and DLS-PBM (green curve) are also included. The calculated molecular mass and fitting error of each peak are indicated in the table below.

**(E and F)** ITC-based measurement of the affinities of the binding of DLS-PBM to PSD-93 (magenta), to SAP102 (blue) and to MAGI-2 (green). The measured binding affinity ($K_d$) and fold change are listed in panel **F**.

In each ITC titration, 200 μM peptide was titrated into 20 μM of different proteins.

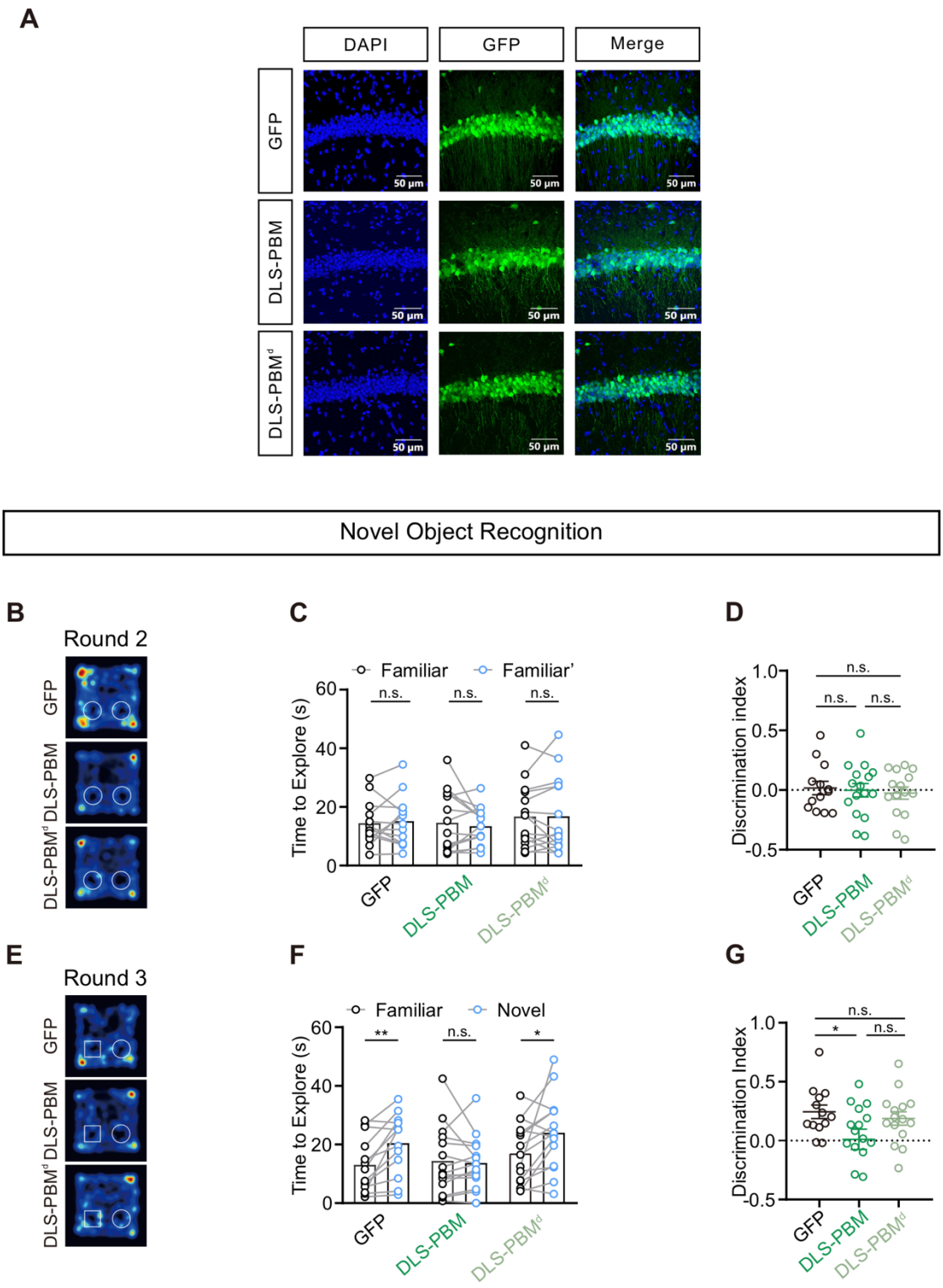


**Figure S2. DLS-PBM causes learning and memory deficits in mice, related to Figure 1.**

**(A)** Representative immunofluorescence images showing the localization of injected virus in the hippocampal CA1 region. Brain sections were stained with DAPI (blue) to label nuclei and GFP (green) to identify the presence of the virus. **(Top row)** GFP-injected control group shows GFP expression in the CA1 region. The merge panel

confirms colocalization of DAPI and GFP signals. **(Middle row)** GFP-DLS-PBM$^{d}$-injected group shows GFP expression indicating viral infection and the presence of the DLS-PBM$^{d}$ peptide. The merge panel confirms colocalization of DAPI and GFP signals. **(Bottom row)** GFP-DLS-PBM-injected group shows GFP expression indicating viral infection and the presence of the DLS-PBM peptide. The merge panel confirms colocalization of DAPI and GFP signals. Scale bars: 50 μm.

**(B)** Representative heatmaps showing the exploration patterns of mice expressing GFP, GFP-DLS-PBM, or GFP-DLS-PBM$^{d}$ groups during the novel object recognition task in Round 2. White circles represent two identical objects.

**(C)** Bar graphs showing the time spent exploring familiar (black) and familiar' (blue) objects in the novel object recognition task during Round 2. Data are presented as mean ± SEM (N = 14-16 number of mice; n.s., not significant; paired t test).

**(D)** The scatter plot showing the discrimination index for the novel object recognition task in Round 2, comparing GFP, GFP-DLS-PBM, and GFP-DLS-PBM$^{d}$ expressing groups. Data are presented as individual values with mean ± SEM (N = 14-16 number of mice; n.s., not significant; unpaired t test).

**(E)** Representative heatmaps showing the exploration patterns of the GFP, GFP-DLS-PBM, or GFP-DLS-PBM$^{d}$ expressing groups during the novel object recognition task in Round 3. White square represents the novel object, and white circle represents the familiar object.

**(F)** Bar graphs showing the time spent exploring familiar (black) and novel (blue) objects in the novel object recognition task during Round 3. Data are presented as mean ± SEM (N = 14-16 number of mice; $^{**}p < 0.01$; $^{*}p < 0.05$; n.s., not significant; paired t test).

**(G)** The scatter plot showing the discrimination index for the novel object recognition task in Round 3, comparing GFP, GFP-DLS-PBM, and GFP-DLS-PBM$^{d}$ expressing groups. Data are presented as individual values with mean ± SEM (N = 14-16 number of mice; $^{*}p < 0.05$; n.s., not significant; unpaired t test).

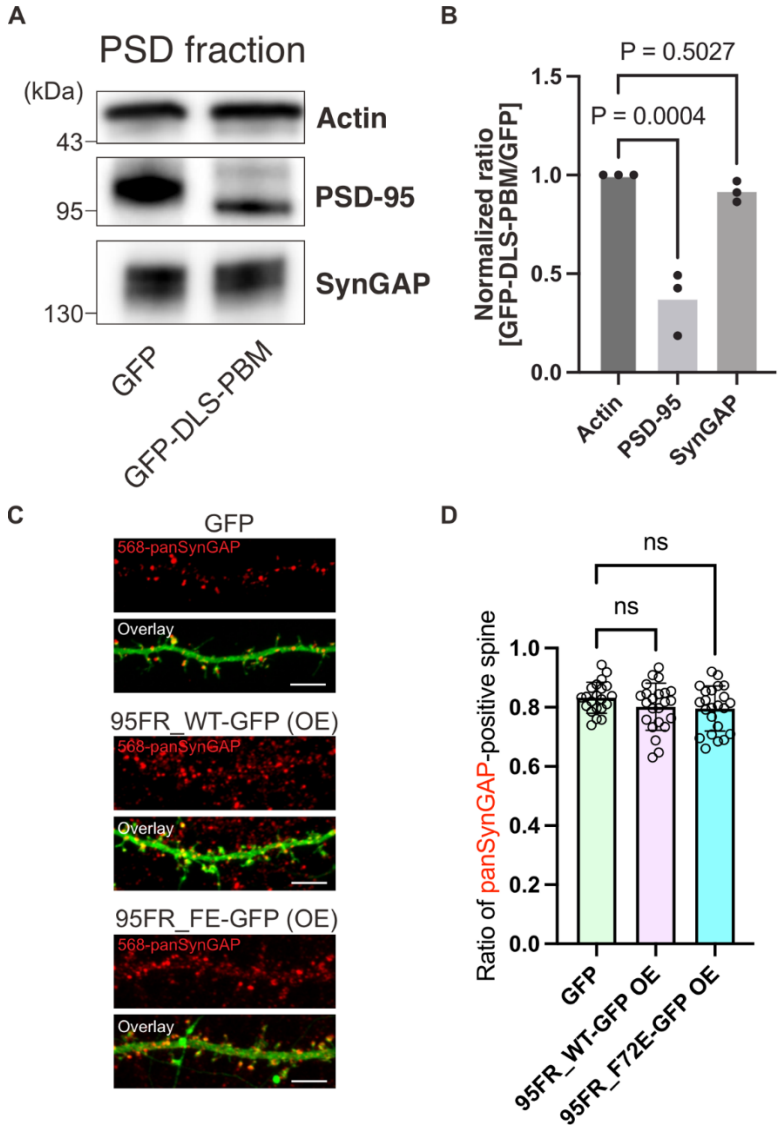


**Figure S3. Expression of the DLS-PBM peptide or PSD-95.FingR (95FR) does not alter synaptic localization of SynGAP, related to Figure 3 and Figure 5.**

**(A and B)** Immunoblot and quantifications show the level of SynGAP did not change in the PSD fraction in cultured neurons expressing the DLS-PBM peptide (with the GFP vector expression as the control). In contrast, the level of PSD-95 was significantly decreased, consistent with the imaging data shown in Fig. 3A-D in the manuscript. The band shift of PSD-95 in the peptide expressing neurons is likely due to its post-translational modification changes. N = 3 independent batches. One-way ANOVA followed by Tukey's post hoc test.

**(C and D)** Panel **C** shows the localization of endogenous SynGAP in cultured neurons expressing GFP, GFP-tagged 95FR_WT or dead mutant 95FR_FE. Most of dendritic spines contained endogenous pan-SynGAP signals in all three groups (quantified in panel **D**). N = 21 (GFP), 23 (95FR_WT-GFP and 95FR_FE-GFP). Data was collected from two independent batches. One-way ANOVA followed by Tukey's post hoc test was applied. ns, not significant. Scale bar: 5 μm.

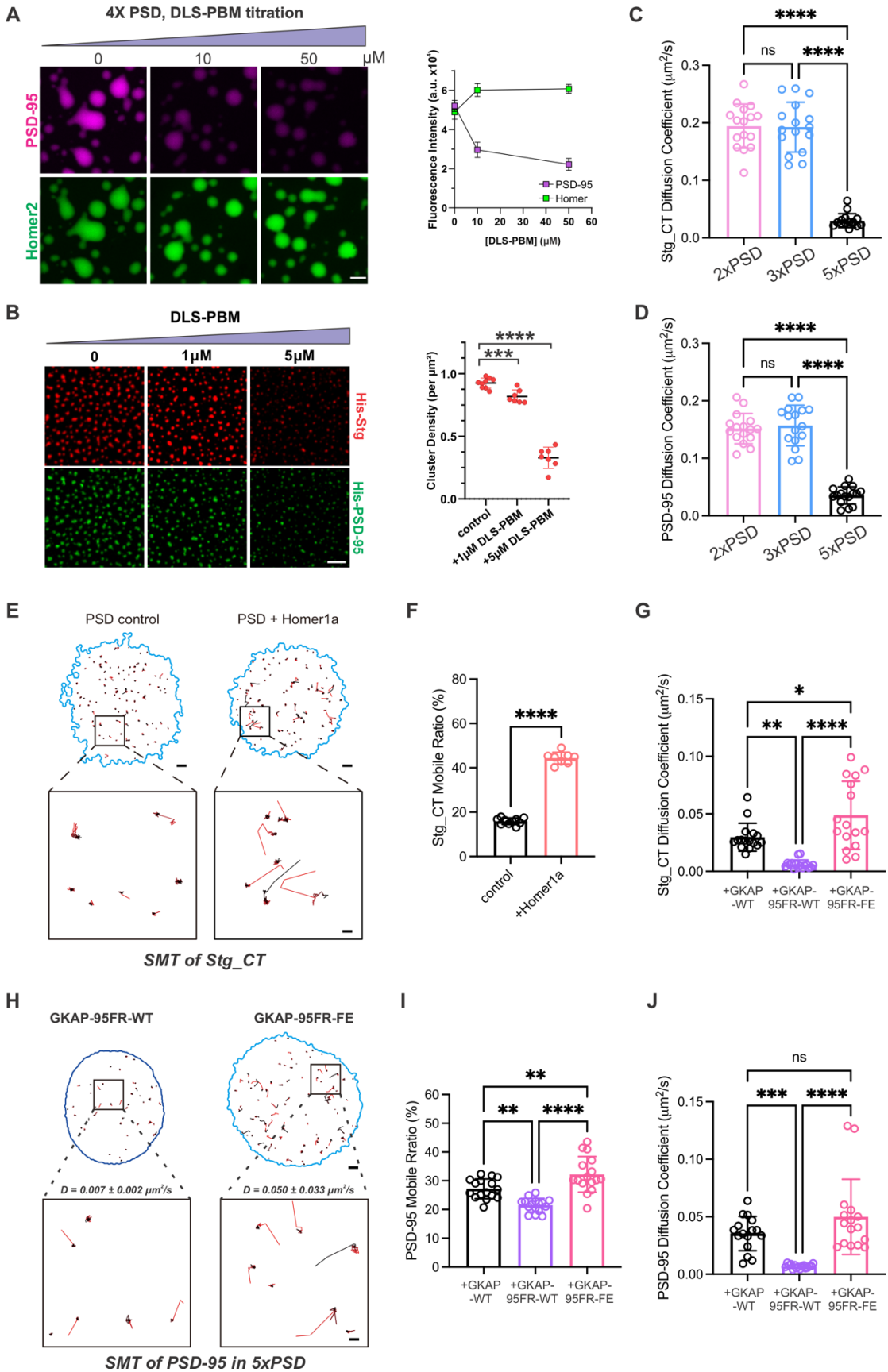
A
4X PSD, DLS-PBM titration
0
10
50
μM
PSD-95
Homer2
Fluorescence Intensity (a.u. x10⁴)
PSD-95
Homer
[DLS-PBM] (μM)
B
DLS-PBM
0
1μM
5μM
His-Stg
His-PSD-95
Cluster Density (per μm²)
control
+1μM DLS-PBM
+5μM DLS-PBM
C
Stg_CT Diffusion Coefficient (μm²/s)
ns
2xPSD
3xPSD
5xPSD
D
PSD-95 Diffusion Coefficient (μm²/s)
E
PSD control
PSD + Homer1a
SMT of Stg_CT
F
Stg_CT Mobile Ratio (%)
control
+Homer1a
G
Stg_CT Diffusion Coefficient (μm²/s)
+GKAP -WT
+GKAP-95FR-WT
+GKAP-95FR-FE
H
GKAP-95FR-WT
GKAP-95FR-FE
D = 0.007 ± 0.002 μm²/s
D = 0.050 ± 0.033 μm²/s
SMT of PSD-95 in 5xPSD
I
PSD-95 Mobile Rratio (%)
J
PSD-95 Diffusion Coefficient (μm²/s)

**Figure S4. Modulating PSD proteins condensation and diffusion behaviors by the DLS-PBM peptide, Homer1a, and GKAP-95FR, related to Figure 4 and Figure 6.**

**(A)** Representative images showing the enrichment of PSD-95 in the PSD condensate formed by the four scaffold proteins: 10 μM PSD-95 (Alexa 647 labelling ratio of 1%), 10 μM pGKAP, 10 μM Shank3 and 10 μM Homer2 (iFluor 488 labelling ratio of 1%). Addition of DLS-PBM peptide causes significant dispersion of PSD-95 from condensate. In contrast, the GKAP, Shank3 and Homer2 (marked by Homer2) condensate remained. Fluorescent intensity quantifications were shown as mean ± SD. N = 8/9/9 droplets for PSD-95 (0/10/50 μM DLS-PBM) and N = 7/10/9 droplets for Homer2 (0/10/50 μM DLS-PBM). Scale bar: 10 μm.

**(B)** Left panel: representative images showing the dispersion of PSD clusters on the membrane in the presence of increasing concentrations of the DLS-PBM peptide. Right panel: quantification of cluster density on the membrane in (I). Data are shown as mean ± SD. n = 9, 7, 7 ROIs for the control, 1 μM DLS-PBM, and 5 μM DLS-PBM, respectively. Unpaired t-test, ***p<0.001, ****p<0.0001.

**(C and D)** Quantification of the apparent diffusion coefficient of Stg_CT (panel **C**) and PSD-95 (panel **D**) in the three types of condensates based on single molecule trajectories from (Fig. 4C-4D). Error bar indicates ± SD. N = 16 droplets for both groups. One-way ANOVA followed by Tukey's post hoc test, ****p<0.0001, ns, not significant.

**(E)** Representative images showing the single molecule trajectories of Stg_CT (Cy3 labelling ratio of 0.035%) from 5x PSD control (10 μM Stg, 10 μM PSD-95, 10 μM pGKAP, 10 μM Shank3-ME and 10 μM Homer2) or 5x PSD adding 250 μM Homer1a. Zoom-in images are used to show examples of single molecule trajectories. Scale bar: 1 μm (up panels), 250 nm (bottom panels).

**(F)** Quantification of mobile ratios of Stg_CT derived from the single molecule trajectories in panel **E**. Error bar indicates ± SD. N = 10, 8 condensates for PSD control and PSD with Homer1a, respectively. Unpaired t test, ****p<0.0001.

**(G)** Quantification of the apparent diffusion coefficient of Stg_CT in the three types of condensates based on single molecule trajectories from (Fig. 4C, Fig. 6B). Error bar indicates ± SD. N = 16 droplets for both groups. One-way ANOVA followed by Tukey's post hoc test, ***p<0.001, **p<0.01, *p<0.05.

**(H)** Representative images showing the trajectories of PSD-95 (Cy3 labelling ratio of 0.035%) from 5x PSD condensates containing 10 μM GKAP-95FR-WT (left panel) or 10 μM GKAP-95FR-FE (right panel). Zoom-in images are used to show examples of single molecule trajectories. The average apparent diffusion coefficient of each group is marked above the representative zoom-in images as mean ± SD. Scale bar: 1 μm (up panels), 250 nm (bottom panels).

**(I and J)** Quantification of the mobile ratios (panel **I**) and apparent diffusion coefficient (panel **J**) of PSD-95 in the three types of condensates based on single molecule trajectories from panel **H** and Fig. 4D. Error bar indicates ± SD. N = 16 droplets for all groups. One-way ANOVA followed by Tukey's post hoc test, ****$p<0.0001$, ***$p<0.001$, **$p<0.01$, ns, not significant.

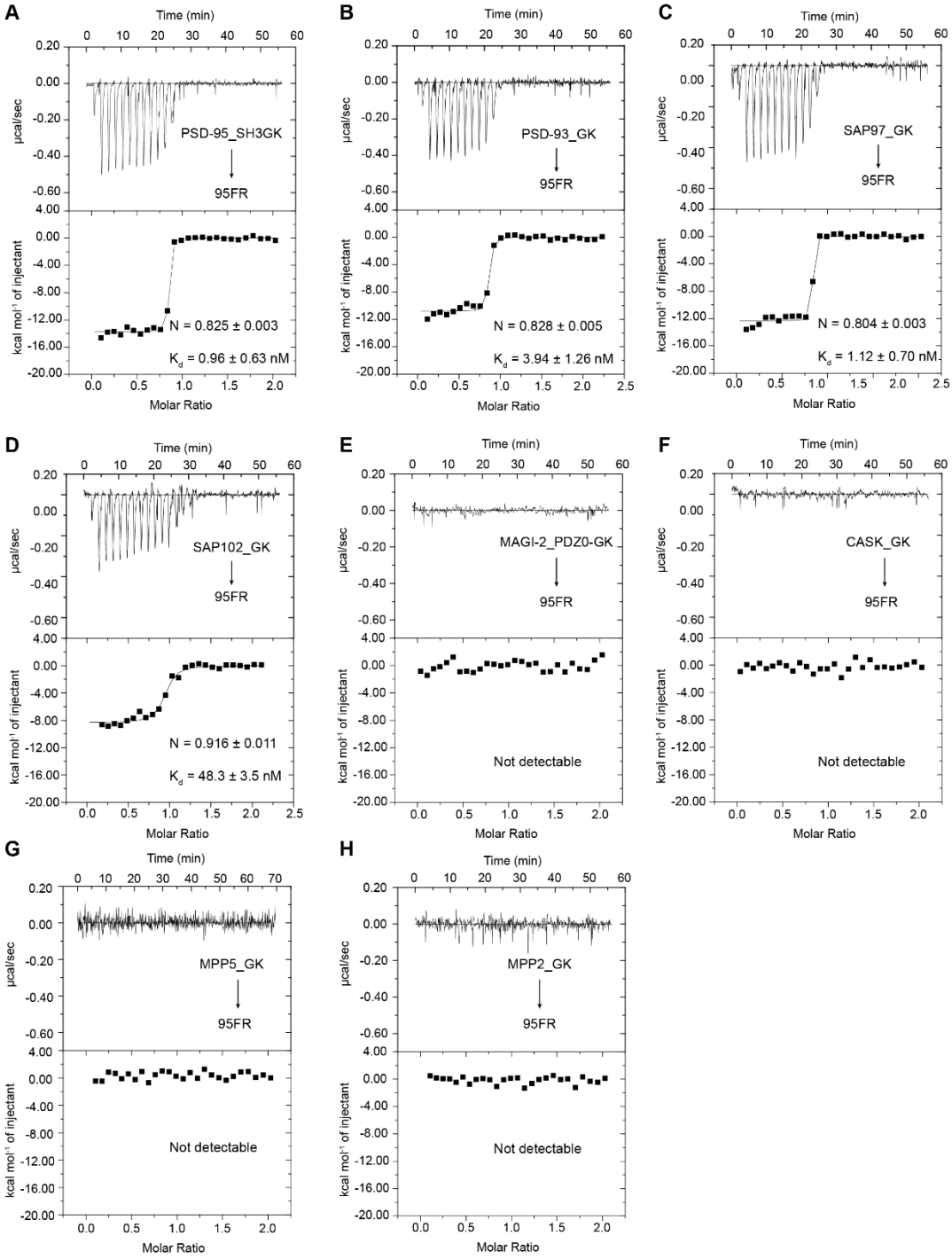


**Figure S5. PSD-95.FingR selectively binds to the GK domains of DLG subfamily MAGUK proteins, related to Figure 5.**

**(A to D)** ITC-based measurements of the binding affinities of 95FR to PSD-95_SH3-GK (panel **A**), to PSD-93_GK (panel **B**), to SAP-97_GK (panel **C**), or to SAP-102_GK (panel **D**). 100 µM GK domain was titrated into 10 µM 95FR in each experiment.

**(E to H)** ITC-based measurement of the binding affinities of 95FR to MAGI-2_PDZ0-GK (panel **E**), to CASK_GK (panel **F**), to MPP5_GK (panel **G**), or to MBP-MPP2_GK (panel **H**). 200 µM MAGUK_GK was titrated into 20 µM 95FR in each experiment.

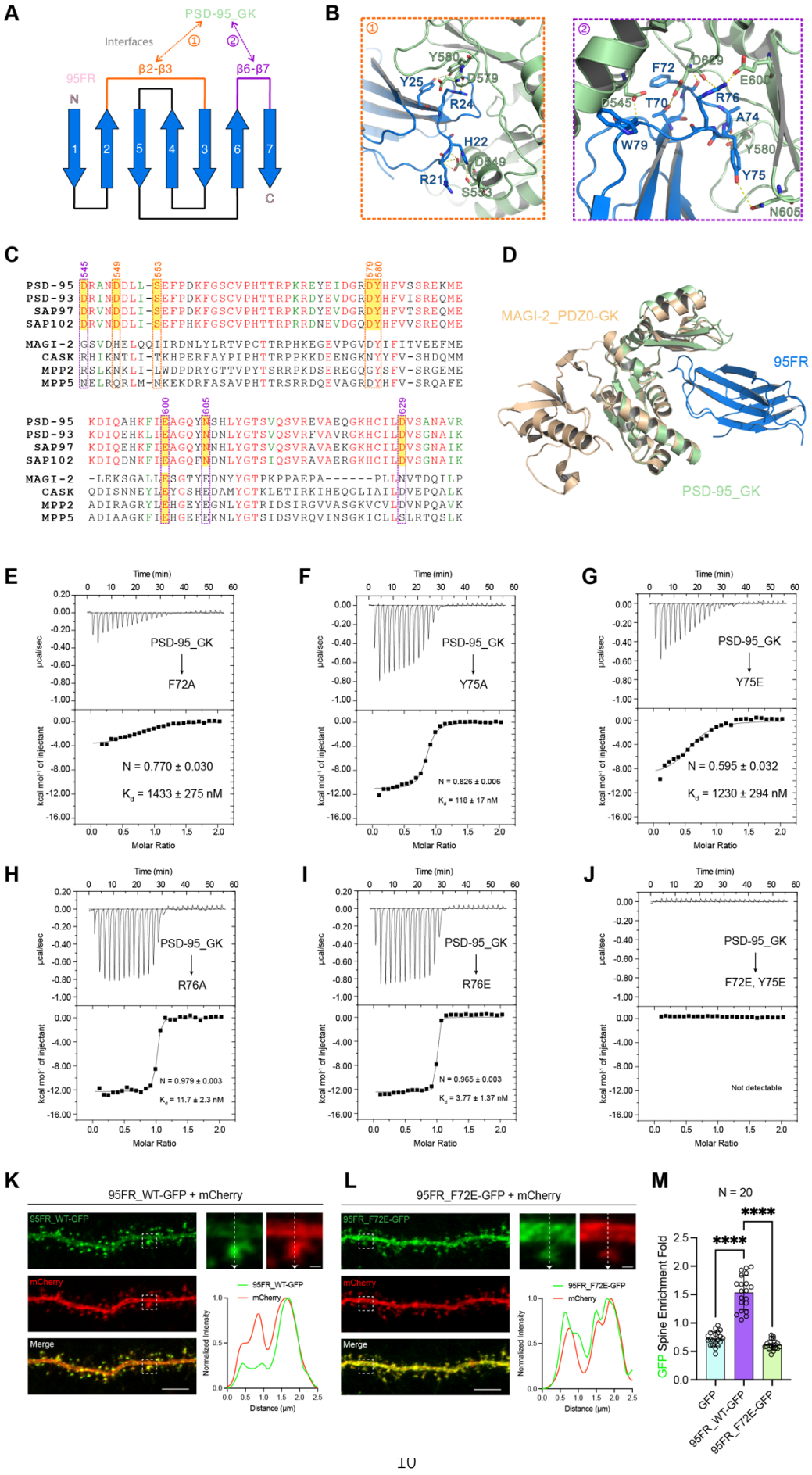
A
PSD-95_GK
Interfaces
β2-β3
β6-β7
95FR
N
C
B
Y580
D579
Y25
R24
H22
D549
R21
S533
F72
D629
E600
D545
T70
R76
A74
W79
Y580
Y75
N605
C
PSD-95
PSD-93
SAP97
SAP102
MAGI-2
CASK
MPP2
MPP5
D
MAGI-2_PDZ0-GK
95FR
PSD-95_GK
E
PSD-95_GK
F72A
N = 0.770 ± 0.030
Kd = 1433 ± 275 nM
F
PSD-95_GK
Y75A
N = 0.826 ± 0.006
Kd = 118 ± 17 nM
G
PSD-95_GK
Y75E
N = 0.595 ± 0.032
Kd = 1230 ± 294 nM
H
PSD-95_GK
R76A
N = 0.979 ± 0.003
Kd = 11.7 ± 2.3 nM
I
PSD-95_GK
R76E
N = 0.965 ± 0.003
Kd = 3.77 ± 1.37 nM
J
PSD-95_GK
F72E, Y75E
Not detectable
Time (min)
µcal/sec
kcal mol⁻¹ of injectant
Molar Ratio
K
95FR_WT-GFP + mCherry
95FR_WT-GFP
mCherry
Merge
Normalized Intensity
Distance (µm)
L
95FR_F72E-GFP + mCherry
95FR_F72E-GFP
mCherry
Merge
Normalized Intensity
Distance (µm)
M
N = 20
****
****
GFP Spine Enrichment Fold
GFP
95FR_WT-GFP
95FR_F72E-GFP

**Figure S6. The PSD-95_GK/95FR complex structure reveals the mechanism underlying the specific binding of 95FR to the GK domains from the DLG MAGUKs, related to Figure 5.**

**(A)** Schematic diagram showing the topology of 95FR and residues from the β2-β3 and β6-β7 loops of 95FR are responsible for binding to PSD-95_GK.

**(B)** The detailed interaction of interface 1 (between the β2-β3 loop of 95FR and GK; left panel) and interface 2 (between the β6-β7 loop of 95FR and GK; right panel).

**(C)** Sequence alignment of GK domains from synaptic MAGUKs tested in Fig. 4B and Fig. S5. The residues that play critical roles in binding to 95FR are highlighted with dashed squares.

**(D)** Superposition of the GK structures from the PSD-95_GK/95FR complex and MAGI-2_PDZ0-GK/pi-SAPAP1-R2 complex (PDB: 7YKI). The chain of pi-SAPAP1-R2 was removed from the aligned structures for easy viewing.

**(E to J)** ITC-based measurements of the binding affinities of PSD-95_GK to 95FR mutants. Panel **E** for F72A; Panel **F** for Y75A; Panel **G** for Y75E; Panel **H** for R76A; Panel **I** for R75E; Panel **J** for the F72E, Y75E double mutant. 200 μM GK domain was titrated into 20 μM 95FR mutants in each experiment.

**(K to M)** Representative fluorescence images showing the localization of 95FR_WT-GFP (panel **K**) or 95FR_F72E-GFP (panel **L**) after 16h of expression in hippocampal neurons. The dashed squares indicate the region selected for the zoom-in views at right. The line scanning plotted the fluorescence intensity distribution following the direction of the dashed arrows. Scale bar: 10 μm and 1 μm for zoom-in panels. Data are quantified in panel **M**. N = 20 for each experimental group (20 neurons from two independent batches). Error bars indicate ± SD. One-way ANOVA followed by Tukey's post hoc test was used. ****P<0.0001.

The detailed interaction between PSD-95_GK and 95FR can be divided into two interfaces, contributed by the β2-β3 loop and the β6-β7 loop of 95FR respectively (Fig. S7A-C). The β2-β3 loop interacts with PSD-95_GK primarily through electrostatic interactions, involving GK_D579-FR_R24 and GK_D549-FR_R21, as well as hydrogen bonds contributed by GK_Y580-FR_Y25, GK_S553-FR_H22, and GK_D549-FR_R21 (Fig. S6B1). On the other hand, the interaction between the β6-β7 loop of 95FR and PSD-95_GK is mediated by a combination of electrostatic interaction (GK_D629/E600-FR_R76), hydrogen bonds (GK_D545-FR_W79, GK_D629-FR_T70/F72 and GK_N605-FR_Y75), and hydrophobic contacts from residues P45, I71, A74, Y75, W79 and P80 of 95FR, to the hydrophobic surface of PSD-95_GK (Fig. 5D and S6C). The above structural analysis was validated by experiments using various mutants of 95FR (Fig. 5B).

Amino acid sequence alignment of GK domains of DLG proteins revealed a high degree of conservation, especially for the key residues that mediate the interaction between GK and 95FR (Fig. S6C), suggesting that 95FR can bind to all four DLG proteins with high affinities. However, sequence comparison between DLG_GK and the GK domains of CASK, MPP2, and MPP5 reveals significant differences in the key residues required for 95FR binding (Fig. S6C). A structure alignment of MAGI-2_PDZ0-GK and PSD-95_GK also revealed a significantly different conformation of the GK domain (Fig. S6D). The above analyses explain why 95FR does not bind to the GK domains of MAGUKs outside the DLG subfamily.

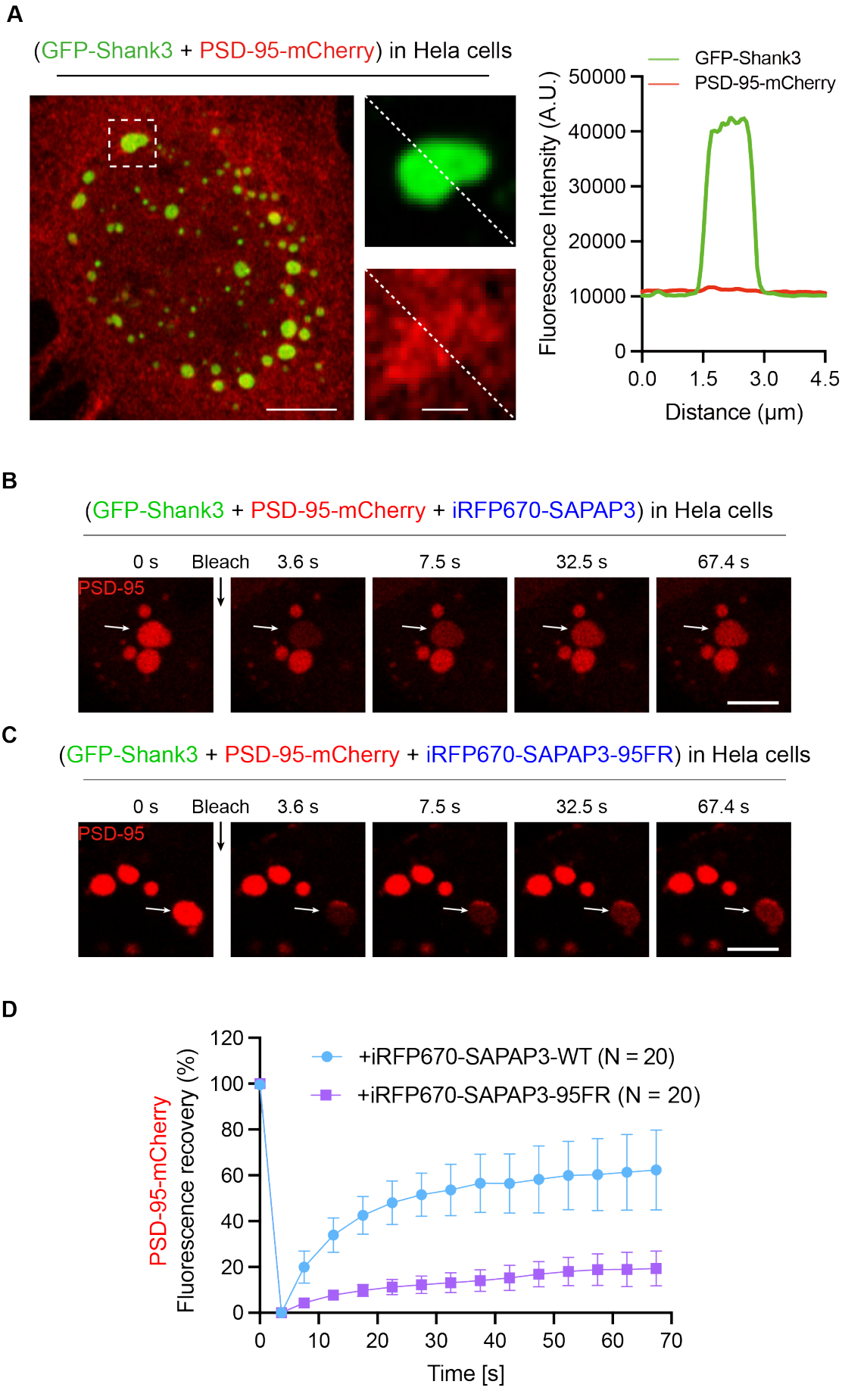
A
(GFP-Shank3 + PSD-95-mCherry) in Hela cells
GFP-Shank3
PSD-95-mCherry
Fluorescence Intensity (A.U.)
50000
40000
30000
20000
10000
0
0.0
1.5
3.0
4.5
Distance (μm)
B
(GFP-Shank3 + PSD-95-mCherry + iRFP670-SAPAP3) in Hela cells
0 s
Bleach
3.6 s
7.5 s
32.5 s
67.4 s
PSD-95
C
(GFP-Shank3 + PSD-95-mCherry + iRFP670-SAPAP3-95FR) in Hela cells
0 s
Bleach
3.6 s
7.5 s
32.5 s
67.4 s
PSD-95
D
+iRFP670-SAPAP3-WT (N = 20)
+iRFP670-SAPAP3-95FR (N = 20)
PSD-95-mCherry
Fluorescence recovery (%)
120
100
80
60
40
20
0
0
10
20
30
40
50
60
70
Time [s]

**Figure S7. PSD-95 enriched into the GFP-Shank3 puncta via SAPAP3-95FR showed the lower dynamics, related to Figure 6.**

**(A)** Fluorescence imaging showing the localization of PSD-95-mCherry and GFP-Shank3 in transfected HeLa cells without SAPAP3 co-expression. No PSD-95 was enriched in GFP-Shank3 puncta. The dashed squares indicate the puncta selected for zoom-in view and line scanning analysis. Line scanning plots of the selected region showing the distributions of PSD-95-mCherry and GFP-Shank3 in the puncta. Scale bar: 5 μm and 1 μm for zoom-in views.

**(B and C)** Representative fluorescence images showing the recovery of PSD-95-mCherry signals after photo-bleaching within the GFP-Shank3 puncta in cells co-expressing and enriching SAPAP3-WT or SAPAP3-95FR. Scale bar: Scale bar: 2 μm.

**(D)** FRAP analysis showing slower dynamics of PSD-95-mCherry in cells co-expressing SAPAP3-95FR compared to cells co-expressing SAPAP3-WT. For each curve, signals were averaged from 20 puncta obtained from different cells.